

Near-Infrared Phototheranostic Iron Pyrite Nanocrystals Simultaneously Induce Dual Cell Death Pathways via Enhanced Fenton Reactions in Triple-Negative Breast Cancer

Chunhua Zhao,[#] Zekun Liu,[#] Chia-Che Chang, Yi-Chia Chen, Qize Zhang, Xiao-Dong Zhang, Chrysfis Andreou, Jiadong Pang, Ze-Xian Liu,^{*} Di-Yan Wang,^{*} Moritz F. Kircher, and Jiang Yang^{*}



Cite This: <https://doi.org/10.1021/acsnano.2c06629>



Read Online

ACCESS |

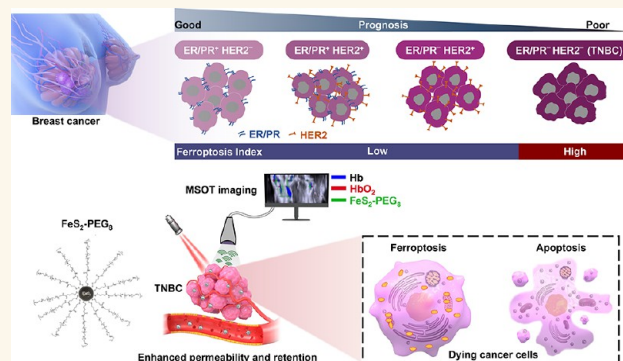
Metrics & More

Article Recommendations

Supporting Information

ABSTRACT: Triple-negative breast cancer (TNBC) is considered more aggressive with a poorer prognosis than other breast cancer subtypes. Through systemic bioinformatic analyses, we established the ferroptosis potential index (FPI) based on the expression profile of ferroptosis regulatory genes and found that TNBC has a higher FPI than non-TNBC in human BC cell lines and tumor tissues. To exploit this finding for potential patient stratification, we developed biologically amenable phototheranostic iron pyrite FeS_2 nanocrystals (NCs) that efficiently harness near-infrared (NIR) light, as in photovoltaics, for multispectral optoacoustic tomography (MSOT) and photothermal ablation with a high photothermal conversion efficiency (PCE) of 63.1%. Upon NIR irradiation that thermodynamically enhances Fenton reactions, dual death pathways of apoptosis and ferroptosis are simultaneously triggered in TNBC cells, comprehensively limiting primary and metastatic TNBC by regulating p53, FoxO, and HIF-1 signaling pathways and attenuating a series of metabolic processes, including glutathione and amino acids. As a unitary phototheranostic agent with a safe toxicological profile, the nanocrystal represents an effective way to circumvent the lack of therapeutic targets and the propensity of multisite metastatic progression in TNBC in a streamlined workflow of cancer management with an integrated image-guided intervention.

KEYWORDS: FeS_2 nanocrystals, ferroptosis, hyperbranched PEGs, multispectral optoacoustic tomography, photothermal therapy, triple-negative breast cancer, breast cancer metastasis



INTRODUCTION

Breast cancer (BC) is a molecularly and histopathologically heterogeneous malignancy, ranking as the most prevalent and the second deadliest cancer among women worldwide. TNBC is a subgroup of invasive BC characterized by the expression absence of the estrogen receptor (ER), progesterone receptor (PR), and human epidermal growth factor receptor 2 (HER2), thus leaving limited therapeutic options and poor prognosis. Worse still, intrinsic or acquired resistance to apoptosis induction further exacerbates the treatment, urging exploration of alternative compensatory death signaling to elicit hybrid pathways.¹ Ferroptosis is an emerging cell death modality that triggers iron-dependent oxidative damage by accumulating lipid reactive oxygen species (ROS).² Transcriptional and translational regulation of iron metabolism cascades, encompassing

iron uptake, storage, and utilization, influences the endogenous labile iron pool (LIP) and dictates the ferroptosis sensitivity through Fenton reactions, which produce excessive ROS.³ Locoregional therapy has successfully made clinical implications in cancer management. Emerging BC local therapeutic regimens, exemplified by lumpectomy and local radiotherapy, are tailored to spare more normal tissues with reduced side effects and conserved cosmetics. However, such approaches

Received: July 6, 2022

Accepted: January 19, 2023

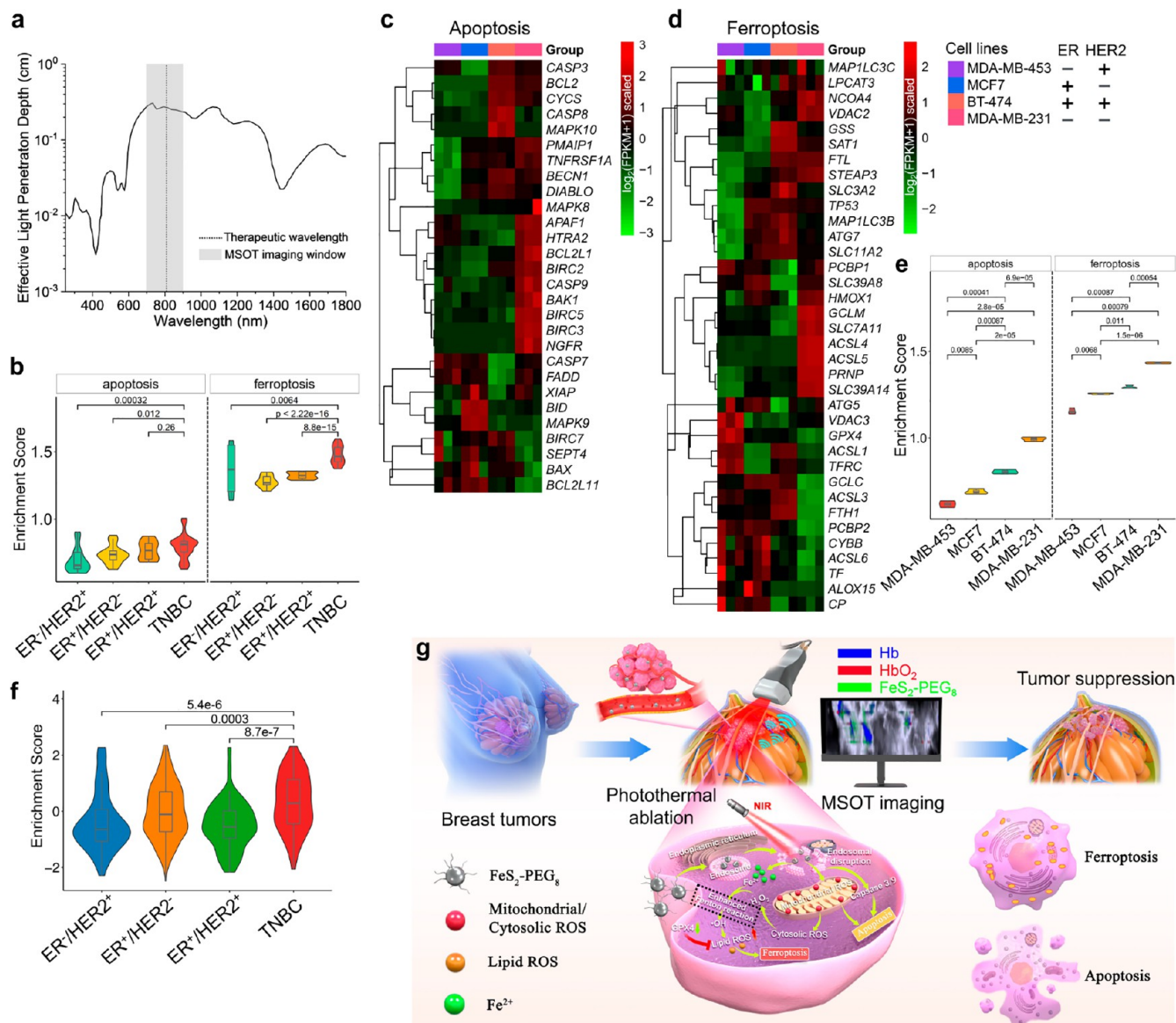


Figure 1. TNBC is more susceptible to ferroptosis with a higher FPI than other breast cancer molecular subtypes. (a) Effective penetration depth in breast tissues as a function of light wavelength. Data were plotted assuming an arterial–venous blood volumetric ratio of 20%:80%. The MSOT imaging window and PTT wavelength are indicated. (b) Enrichment scores of API and FPI among primary molecular subtypes of all human breast cancer cell lines (Cellosaurus cell line database). Statistical analysis was performed using the Wilcoxon test. The mRNA expression profiles of (c) apoptosis and (d) ferroptosis panels for four representative molecular subtypes of human breast cancer cell lines involved in the study. (e) Calculated API and FPI of MDA-MB-453 (ER⁻/HER2⁺), MCF7 (ER⁺/HER2⁻), BT-474 (ER⁺/HER2⁺), and MDA-MB-231 (TNBC). (f) Comparison of FPI among molecular subtypes of human breast cancer tissues. The transcriptomic data were acquired from UCSC Xena, including the TCGA-BRCA cohort. (g) Concept of NIR phototheranostics with Fe₂-PEG₈ NCs. After intravenous injection, Fe₂-PEG₈ systemically circulates and passively targets the tumor through the fenestrated endothelial vasculature by enhanced permeability and retention. Upon cellular entry mediated via electrostatic interactions and macropinocytosis, MSOT imaging visualizes and locates the bulk tumor, followed by photothermal ablation to induce apoptosis and ferroptosis concurrently. All statistical analyses were performed with the Student's *t* test with indicated *P* values.

demand more precise identification of lesions that would inevitably require the assistance of image guidance. For relatively superficial BC, selective photothermal ablation can be achieved noninvasively and locoregionally using less energetic, less tissue-scattered, and deeper penetrative NIR light that can be potentiated by spectrally matched photothermal transduction agents (PTAs). Medical focal laser systems such as the Aveda Health ablation laser and AuroLase have received FDA clearance for cancer treatment. A few representative PTAs have also been developed, including Auroshell and Sebacia

particles in clinical phases or approved. However, most other PTAs reported to date are limited to the preclinical stage and cannot simultaneously attain high photothermal conversion efficiency (PCE) and biological safety.

Multispectral optoacoustic tomography (MSOT) is an advantageous nonionizing hybrid imaging modality merging ultrasound detection and NIR illumination, which circumvents both modalities' drawbacks. However, while MSOT offers label-free molecular specificity of endogenous molecules such as deoxy- (Hb) and oxy-hemoglobins (HbO₂), these molecules

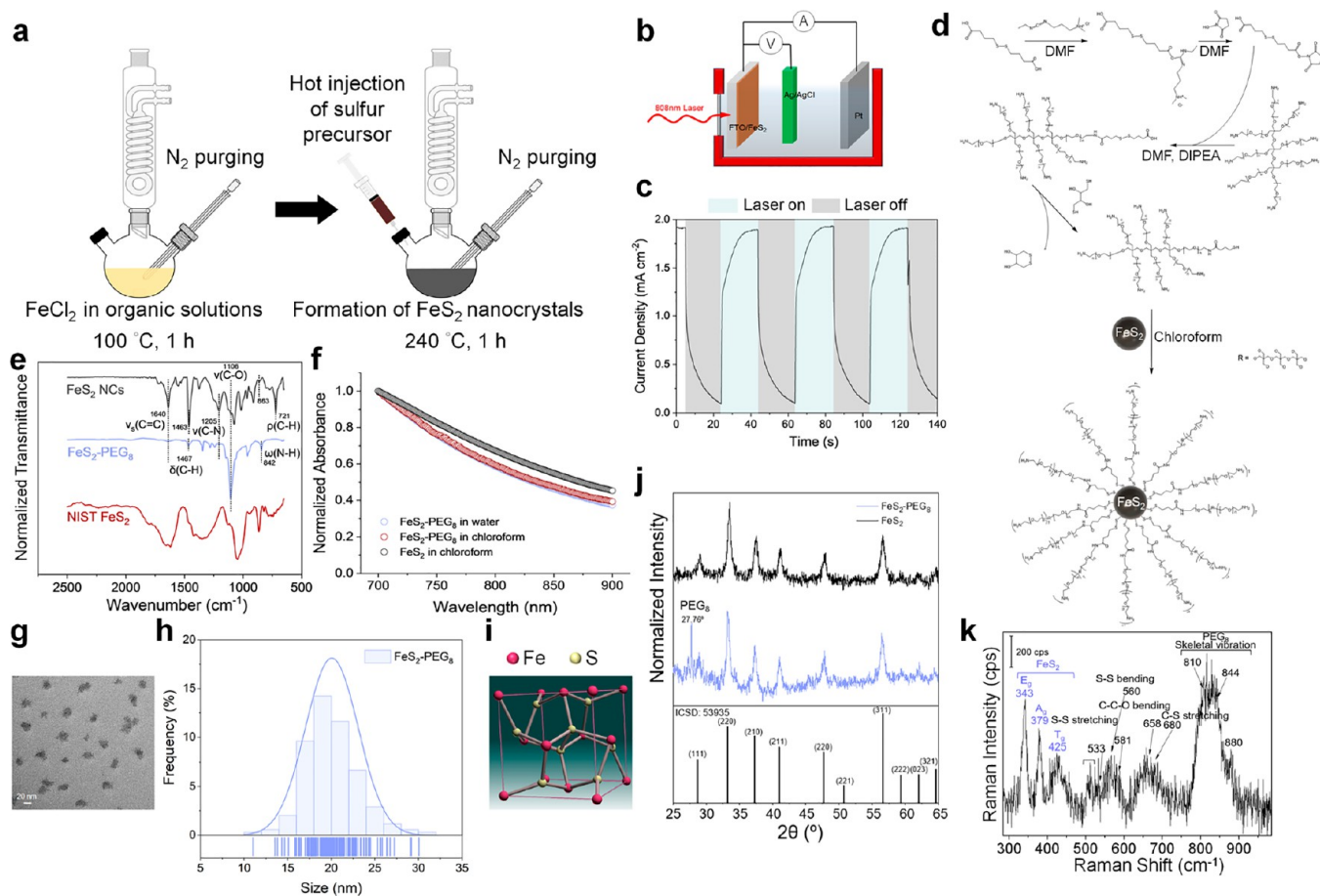


Figure 2. Synthesis and characterization of FeS₂-PEG₈NCs. (a) Schematic of the synthesis process for FeS₂. (b) The three-electrode photovoltaic module consists of FeS₂-coated fluorine-doped tin oxide (FTO) glass, Ag/AgCl, and Pt wire as the working, reference, and counter electrodes, respectively. (c) NIR photovoltaic responses of FeS₂ NCs under on/off cycles of an 808 nm laser illumination at a constant bias of +0.1 V. (d) Chemical modification of FeS₂ NCs with 8-arm PEGs. (e) ATR-FTIR spectra of FeS₂ and FeS₂-PEG₈ NCs. The standard spectrum of iron pyrites (CAS 1309-36-0) retrieved from the National Institute of Standards and Technology (NIST) was referenced. (f) NIR absorption spectra of FeS₂ and FeS₂-PEG₈ NCs. (g) TEM image of FeS₂-PEG₈ with a core size of 20.06 ± 3.03 nm identical to FeS₂ NCs (Supplementary Figure 3a, b; *P* = 0.06). (h) Size distribution of FeS₂-PEG₈ with rug marks. (i) Putative crystal structure of FeS₂ derived from XRD patterns in the JADE software. (j) XRD patterns of FeS₂ and FeS₂-PEG₈ NCs. A matching FeS₂ standard of Inorganic Crystal Structure Database (ICSD) 53935 was included as the reference. Two characteristic peaks around 27° corresponding to PEG₈ can be identified. (k) Raman spectrum of FeS₂-PEG₈.

alone cannot sufficiently reflect the complex physiological and pathological processes in living subjects,³ necessitating the development of extrinsic MSOT contrast agents. On the other hand, MSOT and photothermal therapy (PTT), both requiring nonradiative transitions, are spontaneously complementary, and can be integrated into a streamlined approach using the same phototheranostic agent. An appealing strategy for searching for phototheranostic agents falls in photovoltaic materials with high PCEs extended to the NIR region. Conceivably as an ideal candidate, pyrite is a naturally occurring, earth-abundant, nontoxic, and inexpensive material with a high optical absorption coefficient ($>10^5$ cm⁻¹) and an optimal photoenergy bandgap ($E_g = 0.95$ eV) and has been widely utilized in photovoltaic solar cells. Furthermore, iron sulfides with diverse polymorphs and polytypes are indispensable in biological processes, with the example of iron-sulfur cluster ensembles extensively involved in cell metabolism. More importantly, minor variations in the Fe-S stoichiometric ratios lead to significant changes in structural, chemical, and optoelectronic properties,⁴ making the synthesis of pure phases imperative.

In this study, we synthesized crystalline FeS₂ nanocrystals and exploited an efficient, precisely controlled stoichiometric chemistry to provide aqueous solubility and cationic surface charge to treat TNBC and its metastases. First, one carboxyl group of 4,4'-dithiodibutyric acid (DTBA) was activated into *N*-hydroxysuccinimide (NHS) ester to stoichiometrically favor amide bond formation with a side chain of 8-arm-PEG-NH₂ in the presence of *N,N*-diisopropylethylamine (DIPEA) as a non-nucleophilic organic base. A reactive thiol was then deprotected by 1,4-dithiothreitol (DTT) through S-S bond cleavage, followed by precipitation with diethyl ether and reestablishment of S-S bonds. The prepared FeS₂-PEG₈ has high PCE, serum stability, and photostability, enabling contrast-enhanced MSOT imaging and noninvasive PTT in the biologically "transparent" NIR phototheranostic window of breast tissues (Figure 1a). With the continuous release of redox-active iron(II) species from FeS₂-PEG₈ at local acidic pH that increases the LIP, NIR irradiation effectively accelerates Fenton reactions and raises intracellular radical levels. Subsequently, the ferroptosis switch is turned on as a surplus of caspase 3/9-dependent apoptosis, repressing tumor growth and metastasis *in vitro* and *in vivo* and

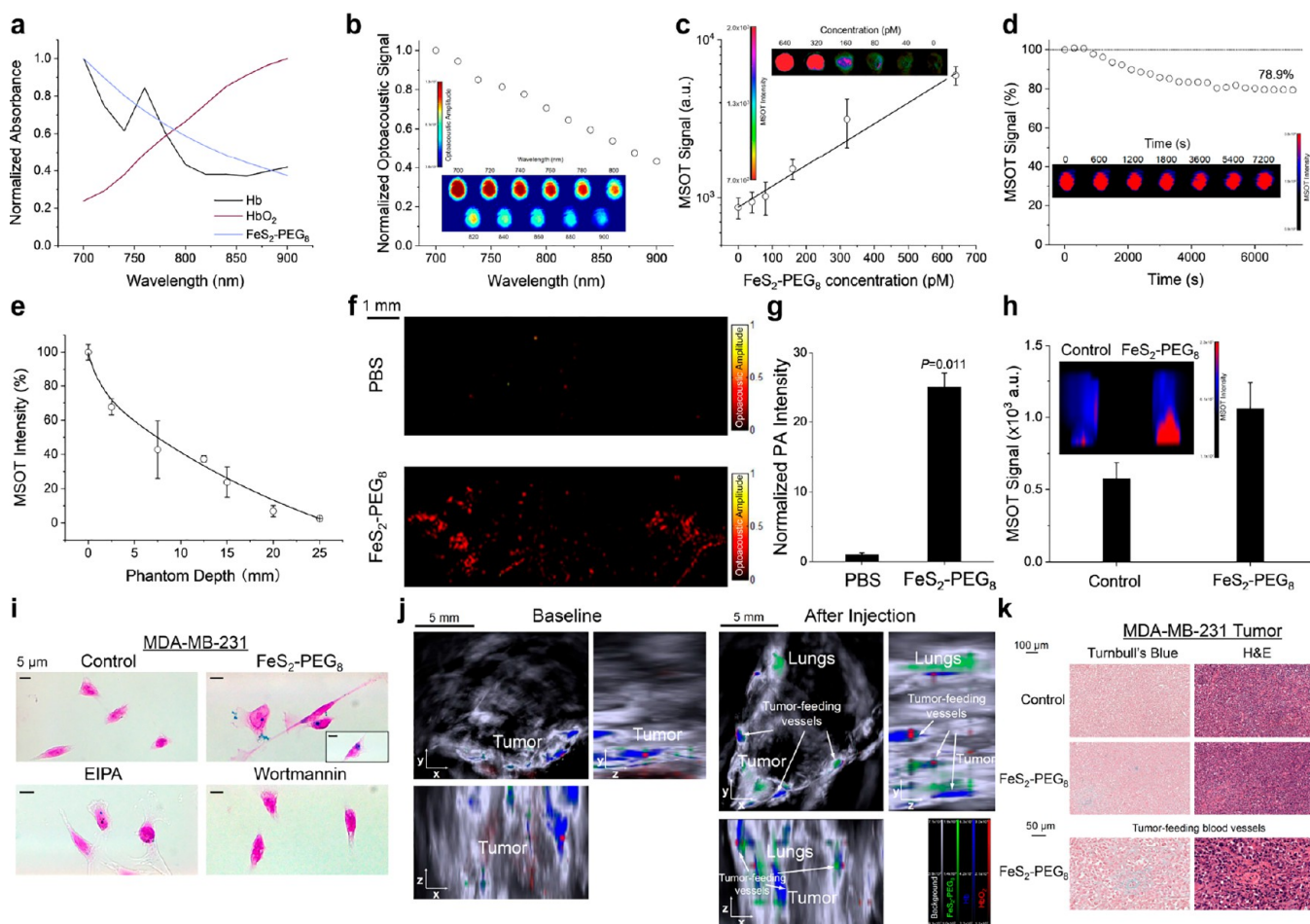


Figure 3. Multispectral optoacoustic tomographic (MSOT) imaging with $\text{FeS}_2\text{-PEG}_8$ NCs in TNBC. (a) Optical spectra for major endogenous photoabsorbers of biological tissues in the NIR region, including Hb and HbO_2 in contrast to the $\text{FeS}_2\text{-PEG}_8$ contrast agent. (b) NIR optoacoustic spectrum of $\text{FeS}_2\text{-PEG}_8$ shares similar features with its absorption spectrum. The inset shows single-wavelength optoacoustic phantom images of $\text{FeS}_2\text{-PEG}_8$. (c) MSOT signals of $\text{FeS}_2\text{-PEG}_8$ in an agarose phantom at gradient concentrations (linear fit $R^2 = 0.991$). (d) MSOT stability. $\text{FeS}_2\text{-PEG}_8$ was subject to continuous spectral sweeping of a pulse laser from 700 to 900 nm. The inset shows representative time-lapse images. (e) MSOT signals of a tissue-mimicking phantom containing $\text{FeS}_2\text{-PEG}_8$ at different imaging depths (exponential decay fit $R^2 = 0.991$). (f) Optical-resolution photoacoustic microscopic (OR-PAM) images of MDA-MB-231 cells after 24 h uptake of 1 μM $\text{FeS}_2\text{-PEG}_8$. (g) Corresponding quantification of OR-PAM intensities. (h) MSOT imaging of MDA-MB-231 cell phantoms with $\text{FeS}_2\text{-PEG}_8$ uptake. (i) Effects of pharmacological inhibitors on the uptake of $\text{FeS}_2\text{-PEG}_8$ in MDA-MB-231 stained by Turnbull's Blue for intracellular Fe(II) species and Nuclear Fast Red for background contrast. (j) Noninvasive in vivo MSOT imaging of xenograft mice bearing MDA-MB-231 breast tumors 1 h after iv injection of $\text{FeS}_2\text{-PEG}_8$. (k) Turnbull's Blue staining of MDA-MB-231 breast tumors resected from xenograft mice 1 h after injection. H&E staining served as the anatomical reference. Fe(II) species primarily accumulated in tumor interstitium and mesenchymal tumor thrombi of blood vessels rather than in the vicinity.

potentially overcoming apoptosis resistance. Such a locoregional NIR photothermal intervention with minimally invasive procedures provides an exciting opportunity, as either single or combinational therapy, for clinicians to ablate unresectable primary and metastatic TNBC tumors under image guidance with perceivable survival benefits.

RESULTS AND DISCUSSION

TNBC Is a Molecular Subtype Sensitive to Ferroptosis with a High Ferroptosis Potential Index (FPI). By computationally establishing bioinformatic models of FPI and apoptosis potential index (API) (Supplementary Tables 1 and 2), we comprehensively analyzed regulatory gene expression profiles of apoptosis and ferroptosis across transcriptomes of primary human BC cell lines (Cellosaurus cell line database). Compared to other molecular subtypes, TNBC cells reveal a differential gene expression pattern of ferroptosis (Supplemen-

tary Figure 1) with a significantly higher FPI (Figure 1b). Meanwhile, the API of TNBC cell lines is also higher than other subtypes, albeit not all with statistical significance. Next, we scrutinized gene expression patterns of apoptosis and ferroptosis in representative model BC molecular subtypes of MDA-MB-453 ($\text{ER}^-/\text{HER2}^+$), MCF7 ($\text{ER}^+/\text{HER2}^-$), BT-474 ($\text{ER}^+/\text{HER2}^+$), and MDA-MB-231 ($\text{ER}^-/\text{HER2}^-$) used in the study. Furthermore, with expression features of regulatory genes (Figure 1c,d), MDA-MB-231 simultaneously manifests the highest API and FPI among all model cell lines (Figure 1e). Similarly, the FPI of human TNBC tissues is higher than non-TNBC counterparts (Figure 1f and Supplementary Figures 2 and 3). Such molecular patterns inspired us to hypothesize that therapeutic activation of dual cell death formats can effectively inhibit the usually recalcitrant TNBC by concurrently arresting primary and alternative survival pathways (Figure 1g).

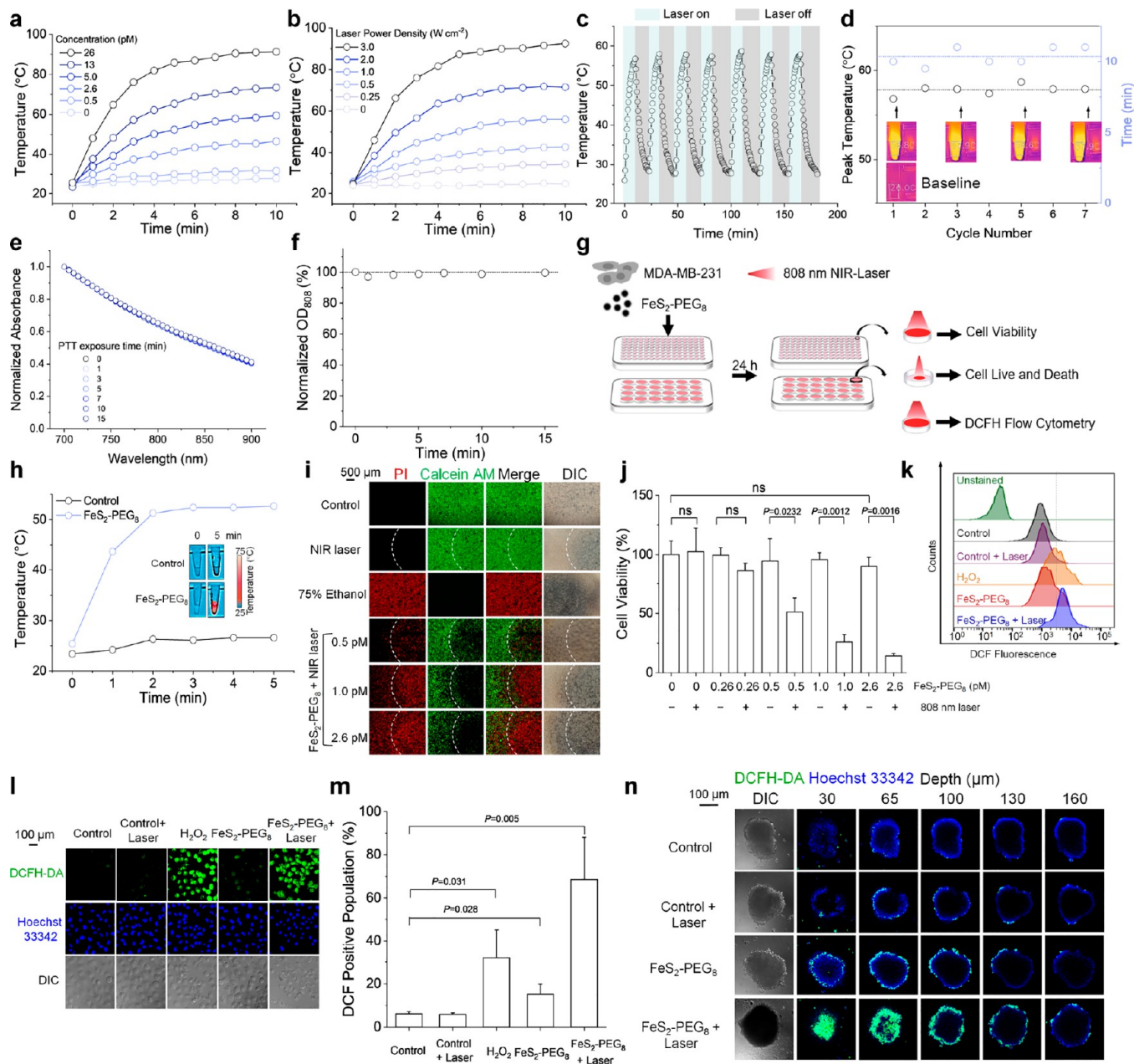


Figure 4. In vitro photothermal therapeutic effects of $\text{FeS}_2\text{-PEG}_8$ NCs against TNBC. (a) Temperature–time curves at different concentrations of $\text{FeS}_2\text{-PEG}_8$ upon continuous exposures to an 808 nm laser of 3.0 W cm^{-2} . (b) Temperature–time curves of $\text{FeS}_2\text{-PEG}_8$ at different laser powers. (c) On-and-off recovery cycles of $\text{FeS}_2\text{-PEG}_8$. (d) Peak temperatures and time durations to reach plateaus at each cycle. The inset shows corresponding thermographic images. (e) NIR absorption spectra of $\text{FeS}_2\text{-PEG}_8$ at different exposure times to the 808 nm continuous laser at 3.0 W cm^{-2} . (f) Optical densities of $\text{FeS}_2\text{-PEG}_8$ at 808 nm as a function of laser exposure time. (g) Schematic illustration for evaluating in vitro photothermal therapeutic effects of $\text{FeS}_2\text{-PEG}_8$ on MDA-MB-231 TNBC cells. (h) Temperature–time curves of MDA-MB-231 cell phantoms upon exposures to an 808 nm laser of 2.5 W cm^{-2} after 24 h cellular uptake of $\text{FeS}_2\text{-PEG}_8$. (i) Live (green)/dead (red) staining by calcein-AM/PI for MDA-MB-231 cells after different treatments. The white dotted lines indicate the boundaries of the imposed NIR laser spot; 75% ethanol was referenced as positive. (j) Cell viabilities of MDA-MB-231 at various concentrations of $\text{FeS}_2\text{-PEG}_8$ in the presence or absence of NIR laser irradiation. (k) Flow cytometry using the DCFH-DA probe for intracellular ROS analysis in MDA-MB-231 cells after different treatments. (l) CLSM and corresponding DIC images of MDA-MB-231 cells stained with DCFH-DA (green) for intracellular ROS and Hoechst 33342 (blue) for nuclei, following treatment as indicated. H_2O_2 served as the positive control. (m) Quantitative analysis of cell populations positive in DCF fluorescence after treatment. (n) CLSM imaging of photothermally triggered ROS distribution at different depths in MDA-MB-231 mammospheres after $\text{FeS}_2\text{-PEG}_8$ uptake.

Synthesis and Characterization of $\text{FeS}_2\text{-PEG}_8$ NCs. To attain the above objective, we first synthesized solution-phase FeS_2 NCs in an O_2 -free organic environment with a Schlenk line (Figure 2a). The NIR photon-harvesting competency of FeS_2 NCs was then justified in a conventional three-electrode

photovoltaic setup (Figure 2b). The responsive photocurrent increased immediately upon 808 nm NIR illumination at a high ratio over the dark current in repeated stable cycles (Figure 2c). Next, we covalently tethered a thiol to the star-shaped amine-terminated hyperbranched 8-arm PEG (PEG_8) through

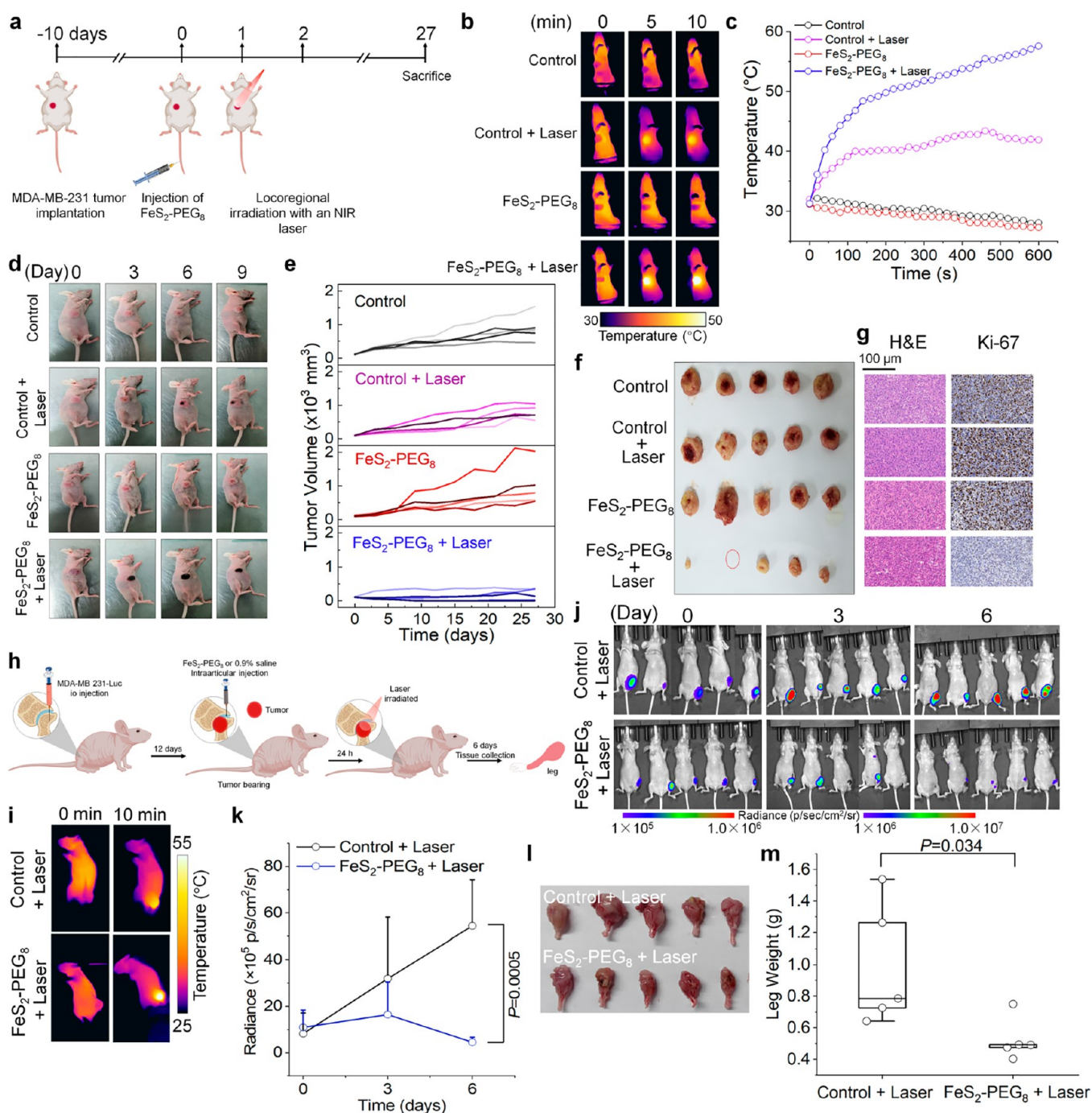


Figure 5. NIR photothermal ablation of TNBC orthotopic and bone metastatic tumors in living mice with FeS₂-PEG₈ NCs. (a) MDA-MB-231 cells ($\sim 5 \times 10^6$) were inoculated through mammary ducts of nude mice at 4–6 weeks of age. On day 10 post-xenografting, mice were randomized into 4 groups ($n = 5$) and iv injected with FeS₂-PEG₈ or 0.9% saline. After 24 h, locoregional irradiation was applied with an 808 nm NIR laser. (b) Thermographic images of xenograft mice bearing MDA-MB-231 TNBC tumors with different treatments at the baseline and various time points of NIR photothermal ablation. (c) Real-time temperature curves of MDA-MB-231 tumors in different groups during photothermal therapy. (d) Representative photographs of xenograft mice bearing MDA-MB-231 TNBC tumors on indicated days after treatment. (e) Individual tumor growth curves of MDA-MB-231 xenografts in different treatment groups. (f) Photographs of excised MDA-MB-231 tumors at the therapeutic end point upon sacrifice. (g) Ki67 IHC and H&E staining of MDA-MB-231 tumor sections after treatment. (h) Experimental process of the establishment and therapeutic scheme for xenograft models mimicking TNBC bone metastasis. (i) Thermographic images of xenograft mice bearing MDA-MB-231 bone metastases at the baseline and with NIR photothermal ablation. (j) Noninvasive BLI and (k) quantified signal intensities of MDA-MB-231 bone metastatic tumors by the expressed Luc reporter on indicated days following treatment. (l) Photographs and (m) weight of resected hind legs with MDA-MB-231 bone metastatic tumors.

precisely controlled stoichiometrical reactions and functionalized FeS₂ via forming disulfide bonds (Figure 2d). Characteristic Fourier-transform infrared (FTIR) bands of FeS₂ NCs,

which are unambiguously different from the reference spectrum of bulk FeS₂ (CAS 1309-36-0), were attributed to capping ligands and diminished after PEGylation (Figure 2e), including

the symmetric C=C stretching at 1640 cm^{-1} , C-H deformation and in-plane rocking at 1463 and 721 cm^{-1} , and C-N stretching of aliphatic amines at 1205 cm^{-1} . Instead, N-H wagging and strong C-O stretching vibrations at 842 and 1106 cm^{-1} from aminated multiarm PEG were present in FeS₂-PEG₈, evidencing successful PEGylation. Furthermore, apart from appended water solubility, FeS₂-PEG₈ showed strong optical absorption in the NIR region with characteristics almost identical in chloroform and aqueous solution, resembling pristine FeS₂ NCs (Figure 2f).

FeS₂ NCs presented a comparable core size of around 20 nm with or without PEG₈ modification (Figure 2g,h and Supplementary Figure 4a,b). In addition, FeS₂-PEG₈ afforded an exceedingly increased hydrodynamic size of 44.7 ± 11.0 nm in a homogeneous dispersion (Supplementary Figure 4c). X-ray diffraction (XRD) disclosed a crystallographic pattern of FeS₂ NCs rigorously matching indexed lattice planes of a FeS₂ pyrite reference standard (ICSD 53935) in a deduced crystal structure centered by a S₂²⁻ pair, with Fe and S atoms in octahedral and tetrahedral assemblies (Figure 2i,j). Following PEGylation, FeS₂-PEG₈ preserved the single-phase pyrite crystallinity and all Raman active modes (A_g, E_g, and T_g) of FeS₂ and featured signature 2θ peaks and skeleton vibrational Raman peaks designated for hyperbranched PEG⁵ (Figure 2j,k). The crystalline size τ of FeS₂-PEG₈ was calculated as 18.6 nm, close to 17.1 nm of FeS₂, according to the Scherrer equation: $\tau = K\lambda/[\beta \cos(\theta)]$, where K is the dimensionless shape factor of the crystal structure, λ is the X-ray wavelength, β is the line broadening at full width at half peak maximum (fwhm) in radians, and θ is the Bragg angle. Furthermore, Raman active vibrations were identified, including C-S stretching and S-S bending and stretching (Figure 2k), substantiating the covalent disulfide linkage between FeS₂ and thiolated PEG₈.

MSOT Imaging of Human TNBC In Vitro and In Vivo with FeS₂-PEG₈. Aminated PEG₈ branches introduce positive charges on FeS₂-PEG₈ at neutral pH (Supplementary Figure 4d), which can readily interact with the anionic proteoglycan-comprised membrane of cancer cells to promote endocytosis.⁶ Meanwhile, FeS₂-PEG₈ NCs retain the stealth effect of PEGylation with high serum stability and low protein adsorption, ideal for in vivo theranostics (Supplementary Figure 5). Moreover, the exogenous optical spectrum of FeS₂-PEG₈ allows definitive differentiation and, thus, spectral unmixing from omnipresent endogenous biological absorbers of Hb and HbO₂ (Figure 3a). Additionally, it bears a strong resemblance to the in vitro NIR optoacoustic spectrum (Figure 3b). The MSOT signal of FeS₂-PEG₈ linearly depended on concentrations in enduring stability, with 78.9% of the original intensity retained after 2 h continuous spectral sweeping (Figure 3c,d). The concrete imaging signal of FeS₂-PEG₈ remained detectable at a deep tissue-mimicking phantom inclusion around 20 mm, though it gradually deteriorated with depth (Figure 3e). Next, we confirmed appreciable intracellular uptake in the model human TNBC MDA-MB-231 by optical-resolution photoacoustic microscopy (OR-PAM) (Figure 3f,g). Similar results were acquired in pelleted bulk cell phantoms using MSOT (Figure 3h). Subcellular localization of FeS₂-PEG₈ was found near the cell membrane and in the cytosol, and effective uptake blockades by specific pharmacological inhibitors validated Ras- and PI3K-dependent macropinocytosis as the predominant endocytic trafficking pathway (Figure 3i).

While similar to the in vitro counterpart, in vivo optoacoustic spectra of FeS₂-PEG₈ following intravenous (iv) injection were

commensurable in the liver, spleen, and lungs (Supplementary Figure 6), which served as the primary distributed organs as corroborated by MSOT imaging and Turnbull's Blue staining (Supplementary Figure 7). Noticeably, negligible distribution was found in kidneys. Besides, specific MSOT signals of FeS₂-PEG₈ were detected in the tumor, lungs, and tumor-feeding blood vessels postinjection (Figure 3j). The tumor enrichment from permeable feeding vessels with discontinuous endothelium was further confirmed by ex vivo histology (Figure 3k). The postinjection distribution profile, particularly in the liver, lungs, and tumor, was quantitatively verified by inductively coupled plasma-mass spectrometry (ICP-MS) (Supplementary Figure 8a,b). FeS₂-PEG₈ facilitated adequate drug exposure ($\text{AUC} = 98\% \text{ID h g}^{-1}$) and a favorable elimination half-life of 5.95 ± 0.70 h, long enough to enforce therapeutic efficacy and avoid frequent dosing but short enough to restrain toxicity from overexposure (Supplementary Figure 8c).

NIR Photothermal Therapeutic Effects of FeS₂-PEG₈ against TNBC and Its Metastasis. In vitro photothermal responses of FeS₂-PEG₈ upon 808 nm NIR excitation effectively elevated temperatures, linearly depending on the concentration and laser power (Figure 4a,b and Supplementary Figure 9). Furthermore, such photothermal effects were sustained in duplicated on-and-off cycles without apparent changes in peak temperatures and time durations to reach plateaus (Figure 4c,d). The PCE was determined to be 63.1% (Supplementary Figure 10), higher than carbon spheres (54.2%),⁷ phthalocyanine-based polymeric micelles (47.0%),⁸ gold nanovesicles (37.0%),⁹ Cu-Ag₂S (58.2%),¹⁰ and dopamine-melanin colloids (40.0%)¹¹ at the same wavelength. Meanwhile, the optical properties of FeS₂-PEG₈ remained principally unaltered with continuous NIR laser illumination (Figure 4e,f). We then conducted a series of cellular assays to examine the in-cell PTT effect after verifying temperature elevation in cell phantoms with FeS₂-PEG₈ uptake (Figure 4g,h). Consequently, FeS₂-PEG₈ induced cell death and decreased cell viability in the presence of NIR light with a concentration correlation (Figure 4i,j). The therapeutic effect augmented intracellular ROS, penetrating in-depth heterogeneous mammospheres (Figure 4k-n).

To evaluate the in vivo therapeutic efficacy, we established TNBC xenograft models, followed by tail-vein injections of FeS₂-PEG₈ (Figure 5a). After applying locoregional NIR irradiation, we found a conspicuous increase in tumor temperatures with a rapid response in seconds, resulting from the intratumoral accumulation of FeS₂-PEG₈ postinjection (Figure 5b,c). Consequently, xenografted TNBC tumors were significantly diminished in size and weight, with lower mitosis, chromatin clumping, and Ki67 expression seen in histology (Figure 5d-g and Supplementary Figure 11a). Importantly, xenograft mice intervened by PTT benefited from extended survival with a steadily increased bodyweight (Supplementary Figure 11b,c).

TNBC is exceedingly invasive, with a high risk of metastasis. To evaluate the therapeutic efficacy of PTT on TNBC metastasis in vitro, we performed transwell cell migration and invasion assays. Upon NIR irradiation, FeS₂-PEG₈ significantly inhibited cancer cell migration and invasion into the extracellular matrix (Supplementary Figure 12). Next, we established human TNBC xenograft models recapitulating metastasis at common sites, including the lungs, lymph nodes (LNs), brain, and bones and applied NIR photothermal ablation (Figures 5h-m and 6; Supplementary Figures 13-16).

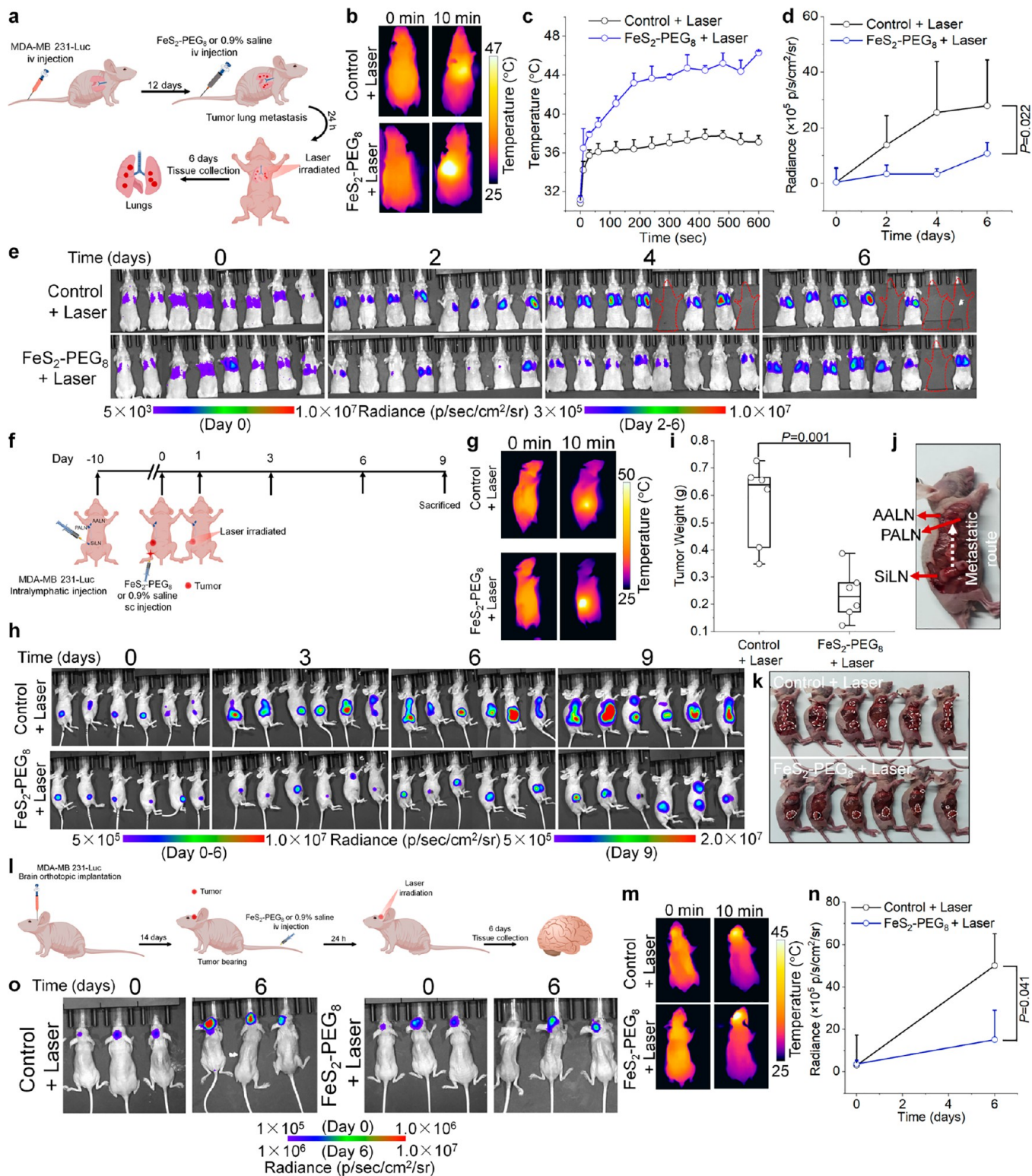


Figure 6. In vivo NIR photothermal ablation of TNBC lung, lymph node, and brain metastases in xenograft mice with FeS₂-PEG₈ NCs. The experimental process of the establishment and therapeutic scheme for xenograft models mimicking TNBC (a) lung, (f) LN, and (l) brain metastases. Thermographic images of xenograft mice bearing MDA-MB-231 (b) lung, (g) LN, and (m) brain metastatic tumors at the baseline and with NIR photothermal ablation. (c) Real-time temperature curves of MDA-MB-231 lung metastatic tumors upon NIR light excitation during PTT. (d) Signal intensities and (e) BLI images of Luc-expressing MDA-MB-231 lung metastatic tumors on indicated days following treatment. (h) BLI images of Luc-expressing MDA-MB-231 LN metastatic tumors on indicated days following treatment. (i) Weight of LN metastatic tumors harvested at the end point of therapy ($n = 6$). (j) An autopsy photograph showing the metastatic routes from the SiLN to PALN and AALN. (k) Representative photographs of xenograft mice bearing MDA-MB-231 LN tumors after treatment. (n) Signal intensities and (o) BLI images of Luc-expressing MDA-MB-231 brain metastatic tumors on indicated days following treatment.

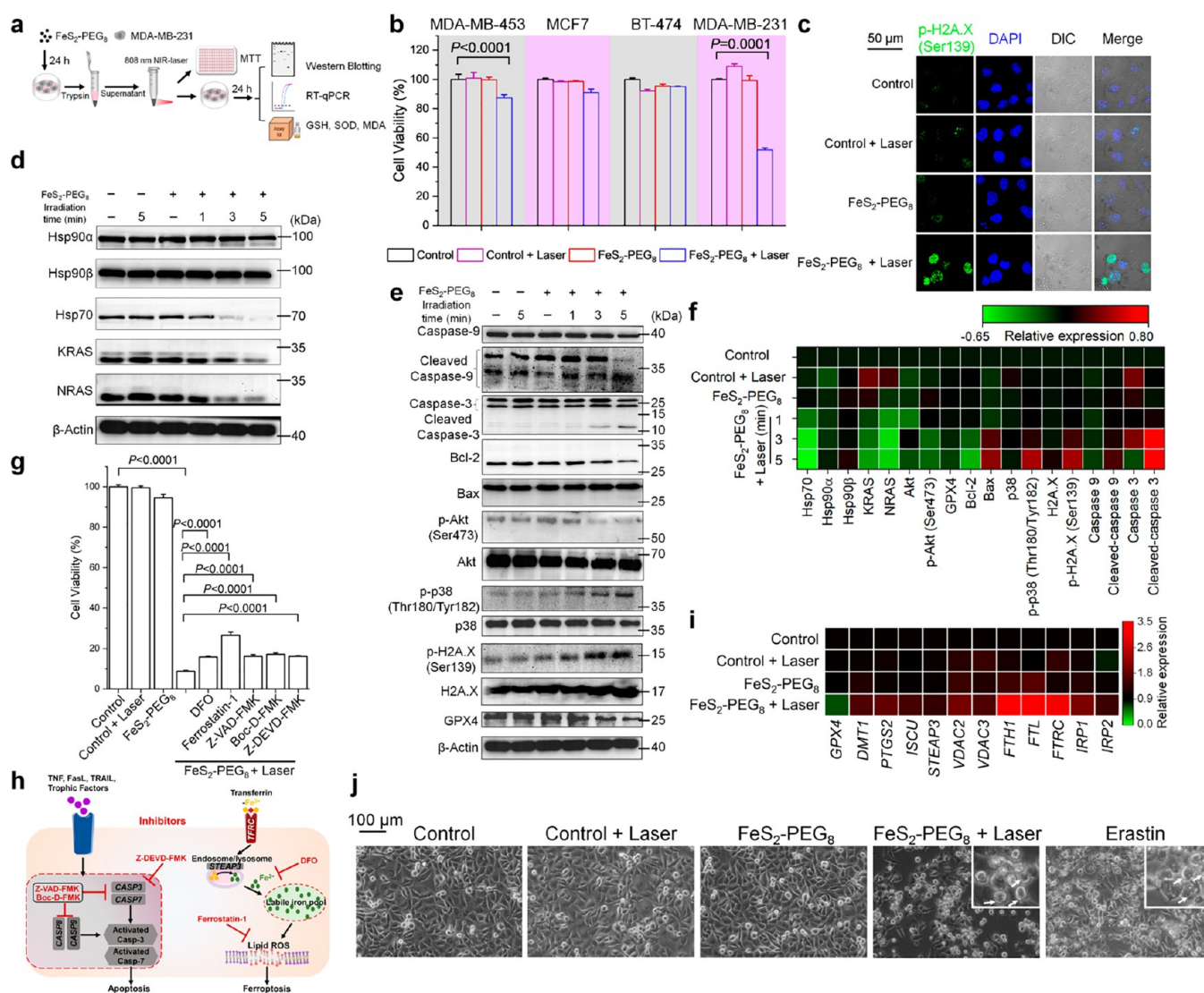


Figure 7. Fe₂-PEG₈ NCs induced dual apoptosis-ferroptosis cell death in TNBC triggered by irradiation of NIR light. (a) Schematic process to study molecular variations from TNBC cell death induced by photothermal treatment with Fe₂-PEG₈. (b) Cell viability assays for different breast cancer molecular subtypes of MDA-MB-453 (ER⁻/PR⁻/HER2⁺), MCF7 (ER⁺/PR⁺/HER2⁻), BT-474 (ER⁺/PR⁺/HER2⁺), and MDA-MB-231 (ER⁻/PR⁻/HER2⁻). (c) Immunofluorescence staining for phosphorylation of histone H2A.X indicating DNA damage. Time-course immunoblotting analysis of (d) major Hsp and Ras proteins and (e) key effectors of the cell-death regulatory signaling pathways in MDA-MB-231 upon NIR laser exposures after 24 h uptake of Fe₂-PEG₈. (f) Heatmap showing quantification of differential protein phosphorylations or expressions for indicated molecules in panels d and e. (g) Effects of apoptosis and ferroptosis inhibitors on the viability of MDA-MB-231 cells after receiving photothermal treatment with Fe₂-PEG₈. Concentrations: 100 μM deferoxamine (DFO), 2 μM ferrostatin-1, 25 μM Z-VAD-FMK, Boc-D-FMK, or Z-DEVD-FMK for 6 h treatment. (h) Schematic illustration summarizing functions of apoptosis and ferroptosis inhibitors used in panel g. (i) Ferroptosis-related mRNA signatures of MDA-MB-231 cells by qPCR with reverse transcription (RT), following photothermal treatment with Fe₂-PEG₈. (j) Phase-contrast microscopic images of MDA-MB-231 cells 24 h after photothermal treatment. Erastin worked as the positive control by inducing ferroptosis.

Thermographic imaging revealed that all metastatic TNBC tumors presented a significantly elevated intratumoral temperature in response to NIR light compared to controls (Figures 5i and 6b,g,m). Consequently, as disclosed by visual inspection, bioluminescence imaging (BLI), and H&E staining, tumor burdens in all metastatic models were significantly suppressed with prolonged survival compared to the control groups (Figures 5h-m and 6; Supplementary Figures 13-16). In addition, among these models, PTT with Fe₂-PEG₈ impeded metastasis from the primary subiliac lymph node (SiLN) to the accessory axillary (AALNs) and para-aortic lymph nodes (PALNs), which occurred through the thoracoepigastric vein and efferent lymphatic vessels (Figure 6f-k and Supplementary

Figure 15). The results corroborate that the therapeutic regimen is effective against primary and metastatic TNBC tumors.

TNBC Is Sensitive to the Caspase 3/9-Dependent Cell Death Induced by Fe₂-PEG₈ under NIR Irradiation. We used diverse biochemical methodologies to elucidate molecularly defined mechanisms underlying Fe₂-PEG₈ as cell death inducers under NIR light (Figure 7a). Out of all BC subtypes, only MDA-MB-231 as TNBC sensitively responded to PTT induced by Fe₂-PEG₈ (Figure 7b), agreeing with the calculated genotype (Figure 1c-e). Accordingly, phosphorylation of histone H2A.X Ser139 was upregulated to form γH2A.X as a prominent indication of DNA double-strand breaks from PTT (Figure 7c). Heat shock proteins (Hsp) are broadly

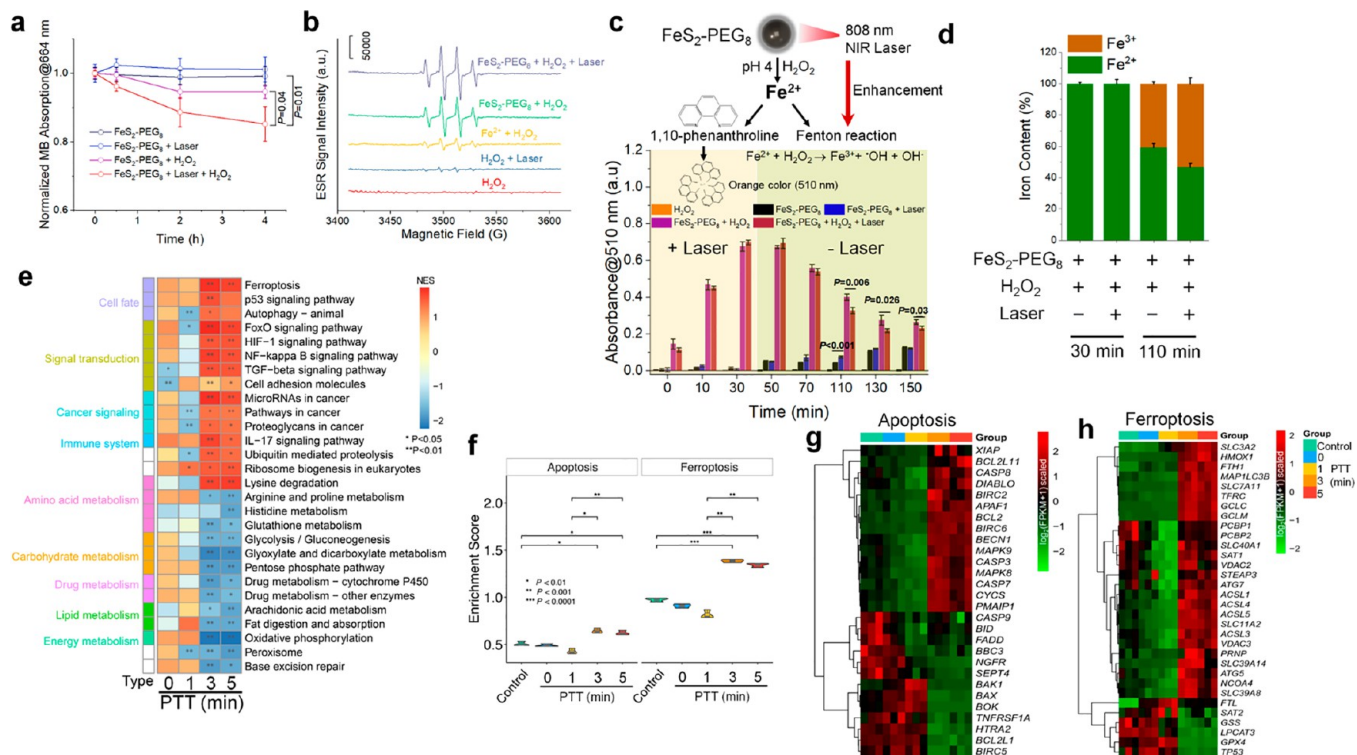


Figure 8. Chemical and molecular mechanisms of the NIR photothermal therapeutic efficacy by $\text{FeS}_2\text{-PEG}_8$ NCs against TNBC. (a) Catalytic decomposition of MB by $\text{FeS}_2\text{-PEG}_8$ in the presence of H_2O_2 through hydroxyl radicals generated from Fe(II)-mediated Fenton reactions. Photothermal effects from NIR light irradiation significantly accelerated the chemical reactions. (b) Electron spin resonance (ESR) spectra to detect the generation of hydroxyl radicals using 5,5-dimethyl-1-pyrroline *N*-oxide (DMPO) as the capturing agent to form DMPO–OH adducts. (c) Transformation of cationic $\text{Fe}^{2+}/\text{Fe}^{3+}$ redox couples in the presence or absence of NIR light at indicated time points. (d) Time-course Fe^{2+} variations in the Fe(II)-mediated Fenton reactions in the presence or absence of NIR light at acidic pH mimicking intracellular vesicles, as detected by the 1,10-phenanthroline probe. (e) Combined identification of enriched GO/KEGG/Hallmark pathways from transcriptomic analyses at different time points post-PTT. (f) Enrichment scores for API and FPI of MDA-MB-231 as a function of the NIR photothermal time with $\text{FeS}_2\text{-PEG}_8$. Time-course differential mRNA expression patterns for (g) apoptosis and (h) ferroptosis in the transcriptomes of MDA-MB-231 after NIR photothermal treatment with $\text{FeS}_2\text{-PEG}_8$.

implicated in cancer thermoresistance, which may attenuate PTT efficacy under stress conditions.¹² To interrogate the effect on major Hsp chaperons, we performed immunoblotting and observed rapid and latent decreases of expression of Hsp70 and Hsp90 α , respectively, but with imperceptible translational changes in the Hsp90 β isoform (Figure 7d). Meanwhile, oncogenic expression of hyperactivated KRAS and NRAS in MDA-MB-231 was attenuated (Figure 7d), responsible for resistance to Hsp90 inhibition.¹³ Likewise, phosphorylation of Akt, p38, and H2A.X was collectively modulated toward proapoptosis with increased cleavage of caspases 3/9 but independent of apoptosis regulators of full-length caspases 3/9 (Figure 7e,f).

$\text{FeS}_2\text{-PEG}_8$ Replenishes the LIP, Enhances Fenton Reactions under NIR Light, and Induces Ferroptosis in TNBC. GPX4, which inhibits ferroptosis and lipid peroxidation, was suppressed at protein and mRNA levels following treatment (Figure 7e, Supplementary Figure 17d). Since regulated cell death could be partially rescued by apoptosis and ferroptosis inhibitors (Figure 7g,h), we thoroughly screened expression of key ferroptosis effectors at transcription levels, which modulate Fe^{3+} reduction to Fe^{2+} , iron metabolism, transport, and storage, ferritinophagy, and antioxidant promoting ferroptosis (Figure 7i and Supplementary Figure 17). Of note, upregulated *FTH1*, *FTHL*, *FTRC*, and *STEAP3* can replenish and expand the accessible LIP with elevated Fe^{2+} storage, thereby increasing

susceptibility to ferroptosis. In the meantime, reduced glutathione (GSH), as a GPX4 cofactor, was depleted under oxidative stress elevated by PTT, while intracellular accumulation of the peroxidation products of polyunsaturated fatty acids (PUFAs), malondialdehyde (MDA), and adapted superoxide dismutase (SOD) escalated with the propagation of lipid peroxidation and ROS generation (Supplementary Figure 18). Further, MDA-MB-231 cells underwent morphological changes of increased membrane densities and ruptures with cellular lipid droplets, similar to erastin-induced ferroptosis (Figure 7j). The augmented LIP engages in generating oxygen-centered radicals through Fenton reactions, promoting lipid peroxidation and ferroptosis. In this study, the production of highly reactive hydroxyl radicals from H_2O_2 via catalysis of $\text{FeS}_2\text{-PEG}_8$ enzyme mimetics was boosted by NIR irradiation (Figure 8a), which decomposed organic pigments like methylene blue (MB). Electron spin resonance (ESR) spectroscopy further confirmed increased adduct formation between $\cdot\text{OH}$ and the spin trapping agent by NIR photocatalysis (Figure 8b). The spontaneous Fe^{2+} release from $\text{FeS}_2\text{-PEG}_8$ was minimal but could be expeditiously facilitated by the nonradical ROS H_2O_2 , with no effects from NIR light (Figure 8c). Concurrently, the released Fe^{2+} was adapted to Fenton reactions in higher consumption that NIR irradiation could drastically accelerate, but higher Fe^{2+} was detected in the absence of H_2O_2 with NIR exposure (Figure 8c).

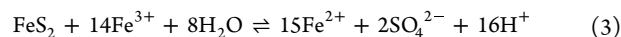
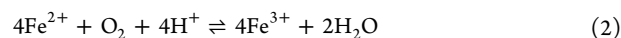
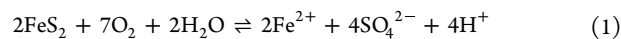
Consequently, a more pronounced Fe^{3+} amount existed as the product of NIR light-enhanced Fenton reactions (Figure 8d).

To pinpoint perturbed gene-function relationships, we performed time-correlated transcriptomic analyses by mapping differentially expressed genes (DEGs) for gene ontology (GO), Hallmark, and Kyoto Encyclopedia of Genes and Genomes (KEGG) enrichment. Overall, DEGs increase in number with irradiation time with functional enrichment in biological terms (Supplementary Figures 19 and 20). Some DEGs were readily differentiated at 1 min, but most were identifiable at 3 min, especially in the signal transduction, signifying cooperative immediate and latent genetic modulations. Enriched slim terms in subhierarchies, with significance levels that increase with time, cover pathways involved in ferroptosis, apoptosis, ROS, and metabolism favoring tumor suppression (Figure 8e). We highlight upregulated p53, FoxO, TGF- β , and HIF-1 signaling pathways, ubiquitin-mediated proteolysis, and autophagy, along with decreased GSH metabolism, peroxisome, and DNA base excision repair, coordinately regulating anticancer efficacy (Supplementary Figures 21 and 22). Moreover, PTT increased API and FPI in differential expression patterns except for 1 min pulse treatment, which implied latent and regulated cell death (Figure 8f–h). Finally, we detailed the time-dependent modulation of key molecular effectors in the ferroptosis cascade (Supplementary Figure 23).

Toxicological Profiling of FeS_2 -PEG₈. Safety is equally vital as efficacy during the treatment of TNBC. Therefore, we evaluated the cytotoxicity of FeS_2 -PEG₈ in both KRAS mutant and wild-type cells, in which toxicity was found to be minimal and independent of macropinocytosis (Supplementary Figure 24). In vitro hemolysis assays with FeS_2 -PEG₈ manifested high hemocompatibility (Supplementary Figure 25). In the meantime, no local or systemic toxicity in the short term was observed with NIR irradiation following injection (Supplementary Figures 26 and 27). Further, no gross abnormality was observed in organs during necropsies upon sacrifice. Subsequent histological examination confirmed the absence of acute and chronic pathological damage within 30 days after injection (Supplementary Figure 28). Pro- and anti-inflammatory gene expression in distributed (spleen, lungs, and liver) and nondistributed (kidneys) organs remained unaltered (Supplementary Figure 29). Broad serum screening of clinical chemistry unveiled transitory elevation in a few electrolytes in the basic metabolic panel that was restored to normal in 30 days (Supplementary Figure 30). By contrast, comprehensive hematological indicators were completely normal, with no meaningful changes in bodyweight (Supplementary Figure 31).

Further Discussion. Key unresolved challenges in current cancer management are (1) efficient elimination of tumors without concomitant off-target tissue damage or systemic toxicities and (2) induction of multiple death pathways that prevent cancer from bypassing and resisting one therapeutic mechanism through alternative survival signaling. Therefore, we proposed a high-precision local-regional NIR photothermal strategy to treat BC under image guidance of the emerging MSOT modality. As a relatively superficial neoplastic malignancy, primary BC is ideal for NIR phototheranostics (Figure 1a). Gleaned from the bioinformatic finding that TNBC is conceivably more inclined toward ferroptosis than non-TNBC (Supplementary Figure 3), we thus aimed to establish an artificial labile iron pool (LIP) beyond the lowest sufficient level and provide excessive cellular availability and abundance to elicit iron dyshomeostasis toward ferroptosis by raising lipid

peroxidation via Fenton reactions. As opposed to oxides, iron pyrite has long been utilized in solar photovoltaics for its superior optical metrics spanning the NIR regions^{14,15} (Figure 2b,c). However, FeS_2 can be vulnerably oxidized by atmosphere O_2 at low pH even before cell entry, as in pyrite weathering and acid mine drainage,¹⁶ following reactions 1–3:



To increase chelatable and redox-active Fe^{2+} in the LIP from cellular uptake of exogenous FeS_2 in the extracellular milieu, we covalently modified FeS_2 NCs with aminated PEG₈ through precisely controlled stoichiometric chemistry to ameliorate hydrophilicity and biocompatibility. The crystallinity and physicochemical characteristics of NCs were well-preserved (Figure 2). The multiarmed hyperbranched PEGs usually have smaller excluded volumes and less freedom of motion with less entropy lost on structural stabilization. More indispensably, the brush conformation diminishes nonspecific protein adsorption and undesirable phagocytic clearance by the mononuclear phagocytic system (MPS) via the stealth effect to achieve prolonged circulation in the bloodstream, EPR-mediated tumor enrichment, and active iron preservation.^{17,18} In the tumor microenvironment, the cationic nature of FeS_2 -PEG₈ from amine protonation allows electrostatic interactions with oppositely charged cell membranes and facilitates efficient RAS-mediated macropinocytotic internalization^{19,20} (Figure 3i, Supplementary Figure 4d). Following cellular entry, sustained Fe^{2+} release is triggered by physiologically occurring H_2O_2 and O_2 at acidic pH of intracellular vesicles and tumor microenvironment, elevating the cellular LIP. Critically, intracellular and in vivo iron species from the immediate release of FeS_2 stay in Fe(II), at least partially or transiently (Figure 3i,k). Meanwhile, NIR irradiation thermodynamically accelerates Fenton reactions to generate $\cdot\text{OH}$ cytotoxic radicals (Figure 8b,c). As in eq 3, the overall redox reaction cycles by self-propagating with lowered pH until depletion of all FeS_2 , using Fe^{3+} produced in NIR-enhanced Fenton reactions as the oxidation agent. Considering that FeS_2 -PEG₈ surpasses the glomerular renal filtration threshold of 30–50 kDa with primary retention in reticuloendothelial systems^{4,5} (Supplementary Figure 7), it serves as a drug depot in vivo and sustains iron release to constitute the cellular LIP.

MSOT with centimeter-scale tissue-penetration depth can dictate intervention planning and accurately resolve tumor anatomic information, including vessels, heterogeneity, and probe distribution with correlative pathological validation²¹ (Figure 3j,k). Benefiting from NIR light-harvesting, FeS_2 -PEG₈ simultaneously actualizes theranostic modalities to enable potential image-guided focal therapy, using contrast-enhanced MSOT to direct the therapeutic laser beam for precise and timely PTT intervention in the operating room. Consequently, it disrupts the antioxidation defense of TNBC cells and coordinately leverages ferroptosis and apoptosis. Hallmarks that define ferroptosis are jointly met with representative morphologies (Figure 7j): failure of damage repair from lipid peroxidation due to repressed GPX4 (Figure 7e–i), sustained availability of the redox-active LIP (Figure 8c), and peroxidation of PUFAs (Supplementary Figure 18c). The induction of dual death mechanisms and multivariate regulation of signaling

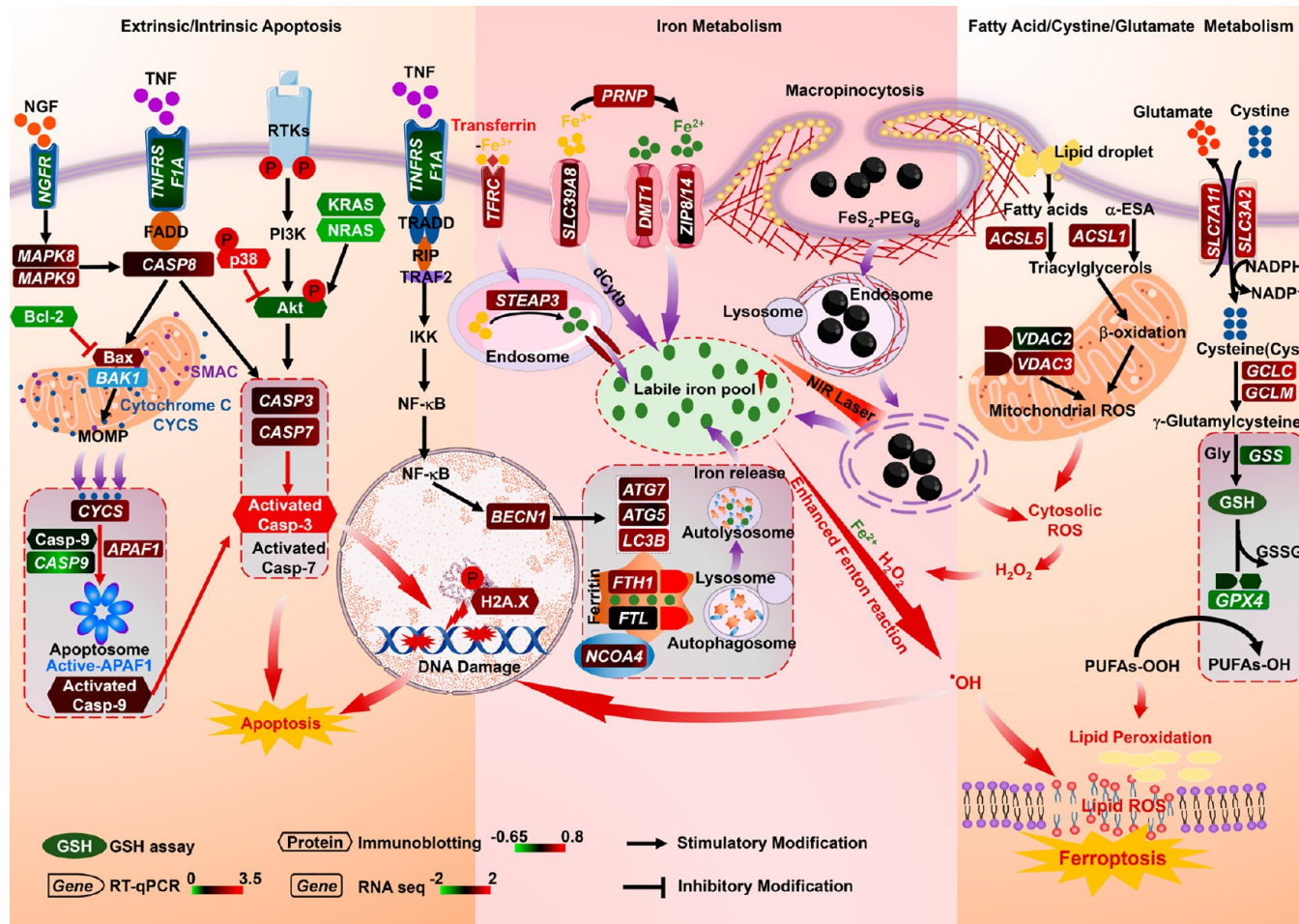


Figure 9. Coordinated signaling pathways for dual programmed cell death regulation by $\text{FeS}_2\text{-PEG}_8$ -mediated NIR photothermal therapy. Data were quantitatively mapped based on immunoblotting, RT-qPCR, RNA-seq, and biochemical assays. Iron uptake mediated by transferrin, SLC39A8 (ZIP8), and DMT1-ZIP8/14 and ferritin degradation mediated by autophagy and lysosome cooperatively liberate reactive iron to replenish the LIP. Excessive cytosolic ROS are generated in TNBC cells upon NIR irradiation in the presence of $\text{FeS}_2\text{-PEG}_8$, resulting from intracellular partitioning of fatty acids and $\alpha\text{-ESA}$ for β -oxidation. Cytotoxic $\cdot\text{OH}$ radicals are then generated from Fenton reactions between LIP and cellular H_2O_2 , causing lipid oxidative stress and ferroptosis. Marked depletion of GSH and GPX4 leads to notable ferroptosis by stimulating lipid peroxidation. Meanwhile, $\cdot\text{OH}$ causes oxidative DNA damage and accumulation of $\gamma\text{-H2A.X}$, denoting apoptosis mediated by TNF-R1 (extrinsic apoptosis) via caspase 8 activation of effector caspases 3/7 as in the study. Moreover, the caspase 8 activation modulates mitochondrial outer membrane permeabilization (MOMP) to release cytochrome c and upregulate Bax. The cascade then regulates the formation of caspase 9 and apoptotic protease-activating factor-1 (Apaf-1) apoptosome complexes to trigger caspase 3/7-mediated apoptosis.

casades impede cancer from escaping death and ensure eradication with combinative mechanisms unveiled (Figure 9). The converged dual pathways potentially overcome cancer refractory to single death pathways. Additionally, the NIR-stimulated thermogenesis of $\text{FeS}_2\text{-PEG}_8$ counteracts intrinsic cancer resistance to stress and dysregulates chaperone functions by downregulating certain HSP expression (Figure 7d). Governed by an overall satisfactory toxicological profile, $\text{FeS}_2\text{-PEG}_8$ conferred moderate near-term fluctuated electrolyte levels, which were subsequently mitigated (Supplementary Figures 30 and 31), possibly attributed to the formation of chalcopyrite-analogous MFeS_x species.²² The NIR phototheranostic paradigm elicits tumor regressive efficacy and safety in treating primary and metastatic TNBC with limited therapeutic receptors.

CONCLUSIONS

To date, interim clinical success in translating focal PTT has been reached with several completed and ongoing trials

(NCT04240639; NCT01679470; NCT00848042) using the FDA-cleared off-the-shelf NIR laser AuroLase paired with the investigational AuroShell agent. Nevertheless, unsolved conundrums persist, including insufficiently explored molecular profiles, unstratified patient populations, limited light penetration, imprecise ablation, and low PCE. To address these challenges, we disclose the ferroptotic susceptibility of the intrinsically heterogeneous TNBC subtype and elucidate the underlying complex regulatory network. Moreover, the highly translatable MSOT modality has been extensively investigated in >10 clinical trials worldwide at various phases. Therefore, we propose a practical theranostic strategy to image TNBC and induce interconnected dual death pathways. Our study reshapes the existing knowledge and expands the capability of FeS_2 , which can readily adapt to other nontoxic NIR-harvesting photovoltaic materials as phototheranostic agents. It can be foreseen that MSOT and PTT can be virtually combined into one integrated hardware to localize cancerous tissues and guide therapies, concurrently fulfilling the “see-and-eradicate” paradigm. BC is a

relatively superficial cancer ideal for locoregional PTT, taking advantage of the penetration depth of up to 5 cm.²³ Hinged on the high PCE and extended NIR spectral absorption of FeS₂, PTT in the NIR second window with lower scattering and absorption may give additional penetration (Figure 1a). FeS₂-PEG₈ NCs may be proposed for stratified TNBC cohorts with iron deficiencies in defined genetic signatures and administered as biologically relevant elements under toxicity thresholds. Potential systemic toxicity risks in humans could be curtailed by minimally invasive intratumoral administration. It ultimately enables an automated end-to-end workflow as the cornerstone to potentiate cancer management. At last, the characterization of intricate molecular events at single-cell resolution, such as transcription, post-transcriptional modification, and translation, is required to corroborate spatiotemporal activations of apoptotic and ferroptotic cascades.

METHODS

Characterization. A JEOL 1200 EX transmission electron microscope (TEM) was operated at 80 kV to visualize nanocrystals on a 300-mesh carbon film-coated copper grid (Electron Microscopy Sciences). X-ray diffraction (XRD) patterns were acquired by a Bruker D8 Advance XRD System, operating with monochromatic Cu K α radiation ($\lambda = 1.5406 \text{ \AA}$) generated at a current of 40 mA and a voltage of 40 keV under a scan rate of 0.01 s^{-1} . UV-vis spectra were obtained with a UV-2600 spectrophotometer (Shimadzu). Fourier-transform infrared (FTIR) spectra were recorded with a Nicolet 6700 spectrometer (Thermo Fisher Scientific) in the attenuated total reflection (ATR) mode. Photoelectrochemical measurements were acquired by an Autolab Potentiostat workstation (Metrohm). Dynamic light scattering (DLS) and zeta potentials were measured with a Zetasizer Nano ZSE Analyzer (Malvern Panalytical). Raman spectra were documented using a UniRAM micro-Raman spectrometer (Nanotech) at the laser wavelength of 532 nm. The concentration of NCs was calibrated by nanoparticle tracking analysis with a NanoSight NS500 system (Malvern Panalytical). Confocal fluorescence images were taken with an inverted LSM880 laser scanning microscope (Zeiss). Thermogravimetric analysis (TGA) was carried out with an STA 6000 Simultaneous Thermal Analyzer (PerkinElmer) from 25 to 800 °C in an argon flow at a heating rate of $20 \text{ }^\circ\text{C min}^{-1}$.

Synthesis of FeS₂ NCs. Unless otherwise stated, all chemicals used for the synthesis of FeS₂ NCs and hyperbranched PEG modification were acquired from Sigma-Aldrich. Ultrapure Milli-Q water (18.2 M Ω cm at 25 °C) was used throughout the study. The synthesis was carried out at a Schlenk line. A mixture of 42 mL containing 1.5 mM FeCl₂ as the iron source, 1.5 mM 1,2-hexadecanediol, 93.9 mM 1-octadecene, and 37.8 mM oleic acid under a continuously purged N₂ atmosphere was maintained at 100 °C for 1 h first to form the iron oleate precursor complex Fe(II) [(9Z)-9-octadecenoate]₁₋₃, followed by immediate injection of a 45.4 mM oleylamine solution containing 18 mM sulfur. The reaction proceeded for 1 h at 240 °C and then quickly cooled to room temperature. The FeS₂ NCs were purified twice with ethanol and transferred into chloroform.

Modification of FeS₂ NCs with Hyperbranched 8-Arm PEG. Three milliliters of dimethylformamide (DMF) with 6.7 mM equimolar *N*-(3-(dimethylamino)propyl)-*N'*-ethylcarbodiimide (EDC) hydrochloride, and NHS was added slowly and dropwise into a 2 mL DMF solution containing DTBA to reach a final molar ratio of 1:1:1. The reaction proceeded under stirring for 30 min at room temperature. Thermodynamically, the low local concentrations of EDC/NHS can activate one carboxyl side chain of DTBA on average into NHS-ester, significantly reducing the chances of activating both side chains. The resulting solution was gradually added drop by drop into a 5 mL DMF solution containing 4 mM 8-arm-PEG-NH₂-HCl (MW 10 000) (tripentaerythritol core) in the presence of 1 mL *N,N*-diisopropylethylamine (DIPEA), which neutralized HCl in the system to stoichiometrically direct formation of amide bonds. The reaction was kept stirring for 24 h at room temperature. An excess of 0.1 g DTT was added

to reduce disulfide bonds in DTBA and reacted for 6 h. Due to its insolubility in diethyl ether, the thiolated PEGs were precipitated, filtered, and redispersed in chloroform, followed by adding a 10 mg mL⁻¹ FeS₂ chloroform solution under sonication for 24 h. The FeS₂-PEG₈ chloroform solution was then dried and stored under a vacuum before aqueous redispersion for further use. The molar concentrations of nanocrystals were experimentally determined by a NanoSight NS300 Nanoparticle Tracking Analyzer (Malvern Panalytical).

NIR Photovoltaic Responses. Fluorine-doped tin oxide (FTO) glass as the substrate was carefully cleaned in a series of steps with a universal neutral cleaner, water, acetone, and isopropyl alcohol. First, an 80 mg mL⁻¹ solution of FeS₂ NCs in DMF was spin-coated onto FTO at 3000 rpm for 60 s. Next, the coated substrate was rinsed sequentially in 2 mM ethanedithiol in acetonitrile and pure acetonitrile. The photoelectrochemical cell in a standard three-electrode setup comprised the Ag/AgCl reference electrode, the Pt wire counter electrode, and the FeS₂ NCs-coated FTO photoanode as the working electrode in a pH 13.5 alkaline SO₃²⁻/S₂O₃²⁻ electrolyte as the sacrificial agent. Finally, an 808 nm NIR continuous laser was applied as the illumination source. Photocurrent responses following NIR light illumination were recorded at a constant bias voltage of +0.1 V as a function of time.

Cell Culture. All cell lines were acquired from the American Type Culture Collection (ATCC). MDA-MB-453 (ER⁻/HER2⁺), BT474 (ER⁺/HER2⁺), and MDA-MB-231 (TNBC) human breast cancer cells were cultured in Dulbecco's Modified Eagle Medium (DMEM). MCF7 (ER⁺/HER2⁻) was cultured in Minimum Essential Media (MEM) with 1 \times NEAA (GIBCO) and 1 \times GlutaMAX (GIBCO). BxPC-3 from human pancreas adenocarcinoma was cultured in RPMI medium as a control. All media were supplemented with 10% fetal bovine serum (GIBCO) with 100 units mL⁻¹ penicillin and 100 μ g mL⁻¹ streptomycin (GIBCO). All cells were grown in a humidified incubator with 5% CO₂ at a constant 37 °C. Trypan blue staining was used for cell counting in PD100 counting chambers read on a Cellometer Auto 1000 automated cell counter (Nexcelom Bioscience). All cells were routinely validated for the absence of mycoplasma contamination using a T100 Bio-Rad Thermal Cycler for polymerase chain reaction (PCR), including the following species: *Mycoplasma hyorhinis*, *M. fermentans*, *M. arginini*, *M. hominis*, *M. orale*, *M. salivarium*, *Acholeplasma laidlawii*, *M. agalactiae*, *M. bovis*, *M. buccale*, *M. arthritis*, and *M. pulmonis*. The oligonucleotide primers specific to the 16S rDNA coding region of the mycoplasma genome are as follows: forward, 5'-TGCACCCTCTGT-CACTCTGTAAACCTC-3'; reverse, 5'-GGGAGCAAACAG-GATTAGTATCCCT-3'.

Cell Viability Assay. Cancer cells ($(1-2) \times 10^4$ per well) were seeded in 96-well plates for overnight incubation, and afterward the medium was replaced with fresh medium containing different concentrations of FeS₂-PEG₈ for a 24 h incubation at 37 °C. After 4 h of further incubation in fresh medium containing 0.5 mg mL⁻¹ 3-(4,5-dimethylthiazol-2-yl)-2,5-diphenyltetrazolium bromide (MTT), 100 μ L of a 10% SDS solution and 0.01 M hydrochloric acid was added to each well for dissolution of formazan crystals. Absorbance at 570 nm was measured using the Infinite M200 Pro multimode microplate reader (Tecan) with 630 nm as a reference. For in-cell PTT, cells after uptake of FeS₂-PEG₈ were irradiated by an 808 nm NIR laser (2.5 W cm⁻²) for 5 min with complete coverage, followed by another 24 h culture before testing. One millimolar sodium dodecyl sulfate (SDS) was used as a positive control. The relative cell viability was calculated according to the following:

$$\text{Cell viability (\%)} = \frac{(\text{OD}_{\text{sample}} - \text{OD}_{\text{background}})}{(\text{OD}_{\text{control}} - \text{OD}_{\text{background}})} \times 100\%$$

Determination of Cellular ROS Activities. MDA-MB-231 cells (5×10^4 per well) were seeded in 24-well plates overnight and treated with 0.1 pM FeS₂-PEG₈ for 24 h. After substitution with fresh media, photothermal treatment was applied using the 808 nm NIR laser at 2.5 W cm⁻² for different periods, followed by an additional 1 h incubation. Cells were trypsinized, collected, and stained with 10 μ M of the cell-

permeant fluorogenic 2',7'-dichlorofluorescein diacetate (DCFH-DA; Sigma-Aldrich) probe for 30 min at 37 °C. After washing, cells were analyzed by flow cytometry with a BD LSRFortessa X-20 Cell Analyzer. Similar procedures were applied to adherent cells in glass-bottomed cell culture dishes (NEST Scientific) for confocal imaging, with additional counterstaining of 5 $\mu\text{g mL}^{-1}$ Hoechst 33342 (Beyotime) to visualize cell nuclei. A positive control with 1 h treatment of 1 mM H_2O_2 was included for reference. Electron spin resonance (ESR) spectroscopy was used to characterize the generation of free radicals, with 5,5-dimethyl-1-pyrroline *N*-oxide (DMPO; Aladdin) as the spin trapping agent. Briefly, 26 pM $\text{FeS}_2\text{-PEG}_8$ and 400 μM H_2O_2 were reacted in pH 4.0 acetate buffer with 97% DMPO added immediately. After NIR photothermal exposure, reactions were transferred into quartz capillaries. X-band ESR spectra were recorded at room temperature in the perpendicular mode on an A300 spectrometer (Bruker). A mixture of 20 mM Fe^{2+} and 400 μM H_2O_2 was set as the positive control.

Immunofluorescence. For immunofluorescence (IF), 2.5×10^5 MDA-MB-231 cells were seeded in a glass-bottomed dish for overnight culture. After incubation in the presence of 1 pM $\text{FeS}_2\text{-PEG}_8$ for 24 h followed by washing, NIR photothermal treatment was applied at 2.5 W cm^{-2} for 5 min, and culture was continued in fresh medium for an additional 24 h. Cells were then washed, fixed in pure methanol for 15 min, and blocked with 3% BSA in PBS for 1 h. Cells were stained in 3% BSA containing 1:400 $\gamma\text{-H2A.X}$ antibodies overnight at 4 °C. After washing, they were further incubated in 3% BSA containing 0.5 $\mu\text{g mL}^{-1}$ 4',6-diamidino-2-phenylindole (DAPI; Beyotime) and a 1:1000 dilution of goat anti-rabbit IgG–Alexa 488 conjugate for 1 h at room temperature, followed by confocal imaging.

Mammosphere Culture. MDA-MB-231 cells (1×10^3 cells per well) were seeded in 6-well Ultralow Adherence plates (Corning) in DMEM/F12 medium containing 20 ng mL^{-1} recombinant epidermal growth factor (GIBCO), 20 ng mL^{-1} basic fibroblast growth factor (R&D Systems), and B-27 supplement (GIBCO), and cultured for 10 days. After incubation with $\text{FeS}_2\text{-PEG}_8$ for 24 h, mammospheres were irradiated with an 808 laser at 2.5 W cm^{-2} and incubated for another 1 h before subsequent dual staining with 10 μM DCFH-DA and 5 $\mu\text{g mL}^{-1}$ Hoechst 33342 for 30 min at 37 °C in the culture incubator. Mammospheres were washed with 1 \times PBS and transferred to a glass-bottomed cell culture dish (NEST Scientific) for imaging.

Intracellular Trafficking of $\text{FeS}_2\text{-PEG}_8$. MDA-MB-231 carrying the KRAS mutation and wild-type BxPC-3 cells were exposed to 5-[*N*-ethyl-*N*-isopropyl] amiloride (EIPA, 150 μM) and wortmannin (100 ng mL^{-1}) for 1 h, which are known pharmacological inhibitors for macropinocytosis and phosphatidylinositol-3-kinases (PI3K), respectively.²⁴ $\text{FeS}_2\text{-PEG}_8$ (20 pM) was added, and the cell culture continued for 12 h. Cells equivalently treated with cell culture-grade dimethyl sulfoxide (DMSO) were incorporated as the control. Intracellular ferrous iron (Fe^{2+}) was visualized by Turnbull's Blue staining. Fixed cells were stained with freshly prepared 30 mM potassium ferricyanide in 6 mM HCl for 2 h at room temperature on an orbital shaker. After washing with 1% acetic acid, Nuclear Fast Red was used for counterstaining.

Animal Models. Protocols for mouse models and procedures in the study were approved by the Institutional Animal Care and Use Committees at Sun Yat-sen University Cancer Center (#L102012020070G) and Memorial Sloan Kettering Cancer Center (#06-07-011), strictly in compliance with NIH guidelines for use and care of laboratory animals. Animals were housed in carefully monitored environmental conditions (food/water supplies, temperature, relative humidity, and 12 h light/dark cycles) and randomly assigned into groups. No additional randomization or blinding procedures were applied. Human xenograft BC models were typically established by subcutaneously inoculating $\sim 5 \times 10^6$ MDA-MB-231 cells through mammary ducts near the third thoracic mammary fat pads of *Foxn1tm/Foxn1tm* mutant nude female mice of 4–6 weeks. Tumor size was calculated with calipers based on the ellipsoid formula: tumor volume = $\pi/6 \times \text{length} \times \text{width} \times \text{height}$. All animals were quarantined for at least a week of acclimatization before starting procedures.

Biodistribution and Pharmacokinetics. Twenty-four hours after iv injection of $\text{FeS}_2\text{-PEG}_8$, xenograft mice bearing MDA-MB-231 tumors were euthanized by CO_2 , with tumors, blood, and major organs (brain, heart, lungs, liver, gallbladder, stomach, spleen, pancreas, kidneys, bladder, skin, muscle, and bone) dissected and collected. All tissues were digested in freshly prepared aqua regia and heated to 100 °C until complete dissolution was reached. The digestion solutions were centrifuged with the supernatants transferred into new 5 mL tubes. The Fe concentration was quantitatively measured using a NexION 1000 ICP mass spectrometer (PerkinElmer). All data were referenced to germanium (Ge) standards and normalized by the injection solution to calculate the percent injected dose per gram of tissue (% ID/g). Similarly, retro-orbital blood was collected from female BALB/cJGpt mice at 12 weeks of age with anesthesia in 20 μL K_2EDTA capillaries at different time points after iv injection for pharmacokinetic analysis by ICP-MS.

Optoacoustic Imaging Setup. MSOT imaging was conducted by real-time scans with the inVision MSOT preclinical system (iThera Medical) for acoustic coupling during measurement, described by us previously.²⁵ In short, NIR optical excitation was sourced from a Q-switched Nd:YAG laser at a pulse duration ≤ 10 ns and a repetition rate of 10 Hz in the NIR range of 680–900 nm. A fiber bundle of ten output arms was used to secure uniform excitation on the imaging plane. Ultrasound emissions were received at a focused 256-element array transducer with a central frequency of 5 MHz. During imaging, the fiber bundle and the transducer elements remained stationary, with the imaged sample moving along the stage during scanning to acquire images in transverse serial planes. In vivo MOST imaging in a water chamber constantly maintained at 34 °C was conducted by iv infusion of 100 fmol $\text{FeS}_2\text{-PEG}_8$ with a catheter into the tail veins of J:NU mice (Jackson Laboratory) bearing palpable human MDA-MB-231 tumors. Xenograft mice were adequately covered with ultrasound gel and wrapped with an optically clear thin polyethylene membrane for optimal acoustic coupling. Acquired 2D MSOT images were reconstructed with the back-projection algorithm in the ViewMSOT software (iThera Medical) and unmixed using a linear spectral model with each image pixel decomposed. Negative values were abandoned, and results were fitted with predefined extinction spectra of deoxyhemoglobin (Hb), oxyhemoglobin (HbO_2), and $\text{FeS}_2\text{-PEG}_8$. Interpolated model-matrix inversion was applied for 3D tomographic reconstruction. Spectrally unmixed images were overlaid to a single-wavelength optoacoustic anatomical reference. Imaging phantoms for mimicking tissue absorption and scattering were prepared in premolded shapes using 1.5% w/w agarose, 1.2% v/v 20% intralipid, and 0.002% v/v India black ink. Tissue-mimicking gels were cut into slices of different thicknesses with a blade in a tissue processing module to study the penetration depth. For microscopic optoacoustic imaging, MDA-MB-231 cells were treated with 1.0 pM $\text{FeS}_2\text{-PEG}_8$ for 24 h and fixed with absolute methanol for 15 min. After washing with PBS three times, cells were collected with cell scrapers and imaged with a home-built VIS-50 optical-resolution photoacoustic microscope (OR-PAM).

Thermographic Imaging. Different concentrations of $\text{FeS}_2\text{-PEG}_8$ in vials were exposed to the 808 nm laser at a power density of 3.0 W cm^{-2} . Infrared thermographic images were taken with a FLIR ONE Pro camera at an interval of 1 min. The temperature was analyzed using the FLIR Tools Thermal Analysis software. Photothermal stability was assessed at continuous irradiation for different durations with UV–vis spectra periodically monitored. The laser was turned off when the temperature reached plateaus and back on when it dropped to ambient temperature to study recovery. The on-and-off cycles were repeated a few times with simultaneous time-lapse thermographic imaging. The photothermal conversion efficiency η was calculated using Roper's model by eq 4:²⁶

$$\eta = \frac{hS(T_{\text{max}} - T_{\text{surr}}) - Q_{\text{dis}}}{I(1 - 10^{-A_{808}})} \quad (4)$$

where T_{max} and T_{surr} are the maximum and surrounding temperatures, respectively, I is the imposed laser power, A_{808} is the absorbance at the irradiation wavelength of 808 nm, Q_{dis} is the heat dissipated from the

solvent to surroundings, and hS is the product of the heat transfer coefficient and container surface area, derived from eq 5:

$$hS = \frac{mC_{\text{H}_2\text{O}}}{\tau_s} \quad (5)$$

where m is the system mass, $C_{\text{H}_2\text{O}}$ is the specific heat capacity of water ($4.2 \text{ J g}^{-1} \text{ }^\circ\text{C}^{-1}$), and τ_s is the sample system time constant calculated from the slope of Supplementary Figure 7 based on eq 6:

$$t = -\tau_s \ln \theta = -\tau_s \ln \frac{T - T_{\text{surr}}}{T_{\text{max}} - T_{\text{surr}}} \quad (6)$$

NIR Photothermal Ablation. In vitro NIR photothermal effects were microscopically evaluated using live/dead staining (YEASEN Biotech). MDA-MB-231 cells (2.5×10^5 cells per well) were seeded in a 12-well plate for overnight incubation, followed by the addition of $\text{FeS}_2\text{-PEG}_8$ for 24 h uptake in culture. Cells were then exposed to a 2.5 W cm^{-2} NIR laser for 5 min, cultured for another 4 h, and double-stained with calcein-AM and propidium iodide (PI) for imaging. Cells treated with 75% ethanol were used as a positive control. In vivo NIR photothermal ablation was accomplished in BALB/cNj-*Foxn1*tm/Gpt nude mice (GemPharmatech) at 4–6 weeks of age bearing MDA-MB-231 breast tumors. Briefly, 5×10^6 MDA-MB-231 cells in $150 \mu\text{L}$ complete culture medium containing 30% v/v Matrigel (Corning) were injected into the subcutaneous breast tissue through the mammary ducts. Tumors were measured using calipers based on the formula of $\pi/6 \times \text{length} \times \text{width} \times \text{height}$. After tumors grew to $\sim 100 \text{ mm}^3$, mice were randomly divided into four groups ($n = 5$) and iv injected with $10.5 \text{ fmol FeS}_2\text{-PEG}_8$ in 0.9% saline. After 24 h, tumors were locoregionally irradiated with the 808 nm laser at 1.6 W cm^{-2} for 10 min. Real-time IR thermographic images were captured during the intervention procedure. After treatment, the tumor size and bodyweight were monitored every 3 days. For Kaplan–Meier survival curves, the end point was defined by tumor sizes $\geq 450 \text{ mm}^3$ or the existence of excessive necrosis. Mice were sacrificed 27 days after the application of PTT.

Transwell Migration and Invasion Assays. MDA-MB-231 cells (5×10^5 cells per well) were seeded in a 12-well plate and treated with $1 \text{ pM FeS}_2\text{-PEG}_8$ for 24 h. Cells were trypsinized, collected, and irradiated with the 808 nm laser. After irradiation, cells were resuspended in 2% FBS-supplemented cell culture media at 1×10^6 cells mL^{-1} . In migration assays, $100 \mu\text{L}$ of cell suspension was directly plated into the transwell insert (Corning) as the apical chamber. Next, $500 \mu\text{L}$ of 12% FBS-supplemented media as the attractant was added to a 24-well plate used as the basal chamber. In invasion assays, $200 \mu\text{L}$ of 0.8 mg mL^{-1} Matrigel in serum-free DMEM was added to the apical chamber of the transwell insert to mimic the structure and function of extracellular matrices. Afterward, $150 \mu\text{L}$ of Matrigel solution was removed immediately, with the rest evenly spread. Then, the transwell insert was incubated at $37 \text{ }^\circ\text{C}$ for 1 h to solidify and seeded with $100 \mu\text{L}$ of the above cell suspension. Likewise, $500 \mu\text{L}$ of 12% FBS-supplemented media was added to the basal chamber, followed by 24 h incubation at $37 \text{ }^\circ\text{C}$. Subsequently, cells were fixed with 4% formaldehyde (Biosharp) for 10 min and stained with 0.1% crystal violet for another 10 min. After extensive PBS washes, excessive cells and Matrigel in the upper compartment were gently removed with a cotton swab. Cell counting was performed by plugging the inset into a new 24-well plate and imaging under a white-light microscope.

Development of Metastatic TNBC Xenograft Models. TNBC commonly favors visceral metastases, such as the lungs and brain, which are nonsuperficial. Therefore, before establishing any metastatic models, we first transduced the luciferase (Luc) reporter system for in vivo cell tracking. Typically, 5×10^6 MDA-MB-231 cells in a 6-well plate were infected by a mixture of $2 \mu\text{g mL}^{-1}$ polybrene and $1 \mu\text{L}$ pLent-EF1a-luciferase-CMV-GFP-P2A-Puro lentivirus (WZ Biosciences) with a titer $> 1 \times 10^8 \text{ TU mL}^{-1}$ and a final multiplicity of infection (MOI) of ~ 20 . After intracellular green fluorescence from the green fluorescence protein (GFP) was observed by wide-field fluorescence microscopy between 24 and 48 h of lentivirus infection, the culture media was removed. To ensure stable expression of the firefly luciferase

gene, we further conducted puromycin selection at 2 mg mL^{-1} over 2 weeks. The resulting cells are termed MDA-MB-231-Luc. Tumor progression in all TNBC metastasis-mimicking models was periodically monitored by BLI via intraperitoneal (ip) injection of 150 mg kg^{-1} D-luciferin (Meilunbio).

For the TNBC lung metastasis model, 1×10^6 MDA-MB-231-Luc cells in PBS were injected into 6-week-old female nude mice via the tail vein. Mice were then randomly divided into two groups and iv injected with $\text{FeS}_2\text{-PEG}_8$ for NIR photothermal ablation after 24 h. In the TNBC LN metastasis model, an incision was introduced in the inguinal area to surgically expose the SiLN from adipose tissues. Next, 5×10^5 MDA-MB-231-Luc cells in $8 \mu\text{L}$ were inoculated by intralymphatic injection. The incision was then closed using sterile surgical sutures. After successful tumor development, $12.5 \text{ fmol FeS}_2\text{-PEG}_8$ in 0.9% saline was injected subcutaneously near the hind leg for therapy after 24 h. In addition, the bone metastasis model was established by intraosseous (io) injection of $10 \mu\text{L}$ of 6×10^5 MDA-MB-231-Luc cells. The needle was inserted under the patella into the anterior intercondylar area to penetrate the tibial growth plate. For the therapeutic regimen, $10 \text{ fmol FeS}_2\text{-PEG}_8$ was injected into the articular, followed by PTT at 24 h postinjection. In the brain metastasis model, a sagittal incision of approximately 1 cm was made with a sterile scalpel to expose the bregma skull. After cleaning with a 3% H_2O_2 solution, the skull was punctured with a sharp syringe at 2 mm left to the bregma and 1 mm anterior to the coronal suture. Next, $5 \mu\text{L}$ of 1×10^7 cells mL^{-1} was slowly injected at 4 mm depth from the skull over 1 min in a perpendicular direction. Finally, the incision was sutured.

Immunoblotting Analysis. MDA-MB-231 cells (1×10^6 cells) were trypsinized and harvested following incubation of 24 h in a medium containing $1 \text{ pM FeS}_2\text{-PEG}_8$. After photothermal treatment (808 nm , 2.5 W cm^{-2}), cells were incubated for 24 h in a fresh medium. Total proteins collected from MDA-MB-231 cells using RIPA Lysis Buffer (Merck Millipore) were quantified and normalized using bicinchoninic acid (BCA) protein assays (Pierce). Proteins were then denatured in 0.04 M dithiothreitol in $1 \times$ NuPAGE LDS Sample Buffer (Beyotime) on a boiling water bath for 10 min and separated by SDS-PAGE. After being blotted onto PVDF membranes (Merck Millipore), they were blocked in 3% BSA for 1 h at room temperature and incubated overnight at $4 \text{ }^\circ\text{C}$ in 3% BSA containing the following primary antibodies at 1:1000 dilutions: anti-Hsp90 α , anti-Hsp90 β , anti-Hsp70, anti- β -actin, anti-KRAS, anti-NRAS, anti-Bax, anti-histone-H2A.X (Proteintech), anti-Bcl-2, anti-caspase-9, anti-cleaved-caspase-9, anti-p-p38 (Thr180/Tyr182), anti-p-histone-H2A.X (Ser139), anti-p38, anti-p-Akt (Ser473), anti-Akt (Cell Signaling Technology), and anti-GPX4 (Santa Cruz Biotechnology). After three times of washing with $1 \times$ Tris-buffered saline with 0.1% Tween 20 (TBST), blots were probed with matched HRP-labeled goat anti-mouse or anti-rabbit IgG (H+L) (Proteintech) for 1 h at room temperature on a shaker and developed in Clarity ECL Western Blotting Substrate (Bio-Rad) for chemiluminescence detection. Bands were visualized using a ChemiDoc Touch Imaging System (Bio-Rad).

In Vitro Hemolysis Assay. Whole blood was drawn by vitrectomy from the vitreous eye cavities of female BALB/cJGpt mice at 8 weeks of age. The whole blood was mixed with PBS and centrifuged at $1000g$ for 10 min to discard the supernatant containing white blood cells and platelets. The pelleted cells were washed three times with PBS and resuspended in PBS to prepare a solution with 2% red blood cells (RBCs). An equivalent mixture from the 2% RBC solution and various concentrations of $\text{FeS}_2\text{-PEG}_8$ was incubated at $37 \text{ }^\circ\text{C}$ for 1 h under 100 rpm shaking. It was then centrifuged at $2000g$ for 5 min with the supernatant subject to optical density measurement at 570 nm . PBS and 0.1% Triton X-100 were the negative and positive controls, respectively. The hemolysis rate was calculated as follows:

$$\text{Hemolysis rate (\%)} = \frac{(\text{OD}_{\text{sample}} - \text{OD}_{\text{negative-control}})}{(\text{OD}_{\text{positive-control}} - \text{OD}_{\text{negative-control}})} \times 100\%$$

Photothermal Damage. Female BALB/cNj-*Foxn1*tm/Gpt nude mice 10 weeks old were iv injected with $10 \text{ fmol FeS}_2\text{-PEG}_8$ in 0.9%

saline. After 1 h, mouse ears, as representative normal tissues, were exposed to 1.6 W cm^{-1} irradiation at 808 nm for 10 min. Photographs were captured to investigate potential photodamage on auricular veins. Twenty-four hours postirradiation, blood was drawn to analyze hematological and clinical chemistry indicators to evaluate near-term adverse effects. Major organs of interest were subject to gross post-mortem examination and collected for fixation in 4% w/v formaldehyde.

In Vivo Toxicity. Female BALB/cJGpt mice of 10–12 weeks were randomly divided into two groups and iv injected with 0.9% saline and $21.0 \text{ pmol FeS}_2\text{-PEG}_8$, respectively. Mice were continuously monitored daily for morbid and mortal signs for a month. Retro-orbital blood was drawn with capillaries on days 14 and 30 postinjection to analyze hematological and clinical chemistry indicators ($n = 3$ for each group and at each time point). In addition, a post-mortem examination of gross organ changes was performed. Freshly dissected organs of interest, including heart, lungs, liver, spleen, pancreas, kidneys, and skin, were collected from euthanized mice and fixed for 24 h in a methanol-free neutral-buffered 4% w/v formaldehyde solution (Biosharp Life Sciences). Fixed organs were processed, paraffin-embedded, and sectioned in $2 \mu\text{m}$ thickness for pathological evaluation with hematoxylin and eosin (H&E) staining. Residual organs were kept in RNAlater solutions (Servicebio) in liquid nitrogen for RNA analysis.

Inflammatory Gene Expression Patterns. Total RNA was extracted from preserved organ tissues with Tissue RNA Purification Kit Plus (RN002plus, ESscience) and quantified using the NanoDrop 2000 spectrophotometer (Thermo Fisher Scientific). Typically, $1 \mu\text{g}$ total RNA was used for cDNA synthesis by reverse transcription (RT) with HiScript II Q RT SuperMix (Vazyme Biotech) that contained buffer, dNTPs, reverse transcriptase, RNase inhibitors, and a primer mix of random primers/oligo-dT. Real-time quantitative PCR (qPCR) was undertaken on a CFX384 Touch Real-Time PCR System (Bio-Rad) using the RealStar Green Fast Mixture (GenStar) containing hot-start Taq DNA polymerase and SYBR Green I to monitor DNA amplification. Primer sequences for inflammation-associated genes are indicated in [Supplementary Table S3](#). Melting curves were constantly monitored to exclude nonspecific products, and expressions were calculated by $2^{-\Delta\Delta\text{Ct}}$ with reference to β -actin.

In Vitro Fenton Reaction. For the Fenton reaction, $4.3 \text{ pM FeS}_2\text{-PEG}_8$ and $66.7 \mu\text{M H}_2\text{O}_2$ were added to a pH 4.0 acetate buffer and incubated at 37°C for 10 min. Next, phenanthroline (Shanghai Aladdin Bio-Chem) dissolved in 20 mM HCl was added at a final concentration of 1.6 mM to detect Fe^{2+} by forming a colorimetric complex. Finally, 808 nm laser irradiation of 3 W cm^{-2} was applied for 5 min, and the reaction was incubated for 120 min. Absorption at 510 nm was measured at a 20 min interval for the content of ferriox complexes.

Degradation of Methylene Blue. Methylene blue (MB) degradation was used as a model to indirectly reflect Fenton reactions by monitoring produced hydroxyl radicals ($\cdot\text{OH}$). Briefly, $100 \mu\text{L}$ of $26 \text{ pM FeS}_2\text{-PEG}_8$ and $50 \mu\text{L}$ of 1 mM MB (Aladdin) were added to $500 \mu\text{L}$ PBS pH 6.5 containing $400 \mu\text{M H}_2\text{O}_2$. Then, a 3 W cm^{-2} 808 nm laser was applied for 5 min, and the reaction was maintained on a shaker for 4 h at 37°C . Afterward, absorbance at 664 nm was measured at predetermined time points to evaluate the effect of NIR light on Fenton reactions.

Cellular Lipid Peroxidation. After NIR photothermal treatment for 3 min at 2.5 W cm^{-2} , 3×10^6 MDA-MB-231 cells were harvested and disrupted using the Bioruptor Pico sonication cell disrupter (Diagenode). Supernatants were collected after 10 min of centrifugation at 3500 rpm. Protein concentrations were quantified by BCA. Cellular contents of reduced glutathione (GSH), superoxide dismutase (SOD), and malondialdehyde (MDA) in response to lipid peroxidation from PTT-generated free radicals were measured spectrophotometrically by kits (Nanjing Jiancheng Bioengineering Institute) and referenced to standards, following manufacturer's instructions.

Histology. After PTT, freshly resected tumors were collected and fixed in neutral buffered 4% w/v formaldehyde fixative for 24 h. Tumors were then embedded in paraffin blocks and sectioned in $2 \mu\text{m}$ thickness for immunohistochemistry (IHC) staining of the proliferation marker Ki67, along with H&E staining as reference. Tissue sections were first

incubated with the rabbit anti-Ki67 polyclonal antibody (Abcam) at 4°C overnight and subsequently with HRP-conjugated goat anti-rabbit IgG for 1 h at room temperature. Finally, it was developed with a rabbit-specific HRP/DAB IHC Detection Kit (Abcam). Turnbull's Blue staining pathologically detected tissue ferrous iron (Fe^{2+}). Tissue sections were deparaffinized in a series of xylene and ethanol concentration gradients, followed by hydration in distilled water. Slides were stained with freshly prepared 30 mM potassium ferricyanide in 6 mM HCl overnight and washed extensively with 1% acetic acid. Counterstaining was achieved using Nuclear-Fast Red for 5 min to provide tissue contrast.

Ferroptosis-Related Gene Signatures. After incubation in $1 \text{ pM FeS}_2\text{-PEG}_8$ for 24 h, MDA-MB-231 cells were subject to NIR laser exposure at 2.5 W cm^{-2} for 3 min. Cells were further incubated in a fresh medium for 24 h. Cellular RNA was extracted using an RNA Quick Purification kit (Shanghai Yishan Biotechnology) and quantified with Nanodrop. As the above, cellular ferroptosis-related mRNAs were determined by qPCR with RT. Primer sequences are displayed in [Supplementary Table S4](#).

RNA Sequencing. MDA-MB-231 cells (5×10^6) were incubated with $1 \text{ pM FeS}_2\text{-PEG}_8$ for 24 h and exposed to 2.5 W cm^{-2} NIR illumination for 1, 3, and 5 min. Treated cells were further incubated in freshly replaced media for another 24 h, harvested and extracted for RNA with 3 mL TRIzol (Invitrogen). The total RNA was purified and reverse-transcribed into cDNA with SuperScript II Reverse Transcriptase (Invitrogen). $2 \times 150 \text{ bp}$ paired-end sequencing (PE150) was performed on an Illumina Novaseq 6000 sequencing platform (LC-Bio Technology).

Bioinformatics. The raw sequencing data from RNA-seq were mapped to the human reference genome (UCSC GRCh38). HISAT v2.0⁷⁷ and StringTie v1.3.4²⁸ were applied to quantify gene expression. Expression matrices for raw read counts and transcripts per million (TPM) were constructed for all samples. Differential expression analysis was performed using the R package DESeq2 v1.20.0,²⁹ and genes with $\log_2(\text{fold change}) > 1$ and adjusted p -values < 0.05 were defined as DEGs. Gene set enrichment analysis (GSEA)³⁰ was performed using GSEapy (<https://github.com/zqfang/GSEapy>), a python version software of GSEA. Gene sets from Gene Ontology (GO, <http://geneontology.org/>), Kyoto Encyclopedia of Genes and Genomes (KEGG, <https://www.genome.jp/kegg/>), Reactome (<https://reactome.org/>) as well as Hallmarks were downloaded from MSigDB (<http://www.gsea-msigdb.org/gsea/msigdb/>) and were all taken into consideration for GSEA. Gene expression visualization in pathways was performed on the web server Pathview.³¹ The transcriptome data sets of breast cancer cell lines were obtained from GSE66071.³² The transcriptome data sets of breast cancer tissues were retrieved from UCSC Xena (<https://xenabrowser.net/datapages/>), including the TCGA-BRCA project³³ and Yau's research.³⁴ To compare the pathway activities among groups, we used the R package GSVA and the 'ssgsea' method to calculate the enrichment scores as FPI and API of ferroptosis and apoptosis pathways with gene lists downloaded from KEGG.³⁵

ASSOCIATED CONTENT

Data Availability Statement

Data for figures in the study are deposited in the *Research Data Deposit* (RDD) public medical research database with the identifier RDDB202225724. Customized R codes for bioinformatic analysis are available from the authors upon request.

Supporting Information

The Supporting Information is available free of charge at <https://pubs.acs.org/doi/10.1021/acsnano.2c06629>.

Ferroptosis and apoptosis regulatory genes for index calculation; primer sequences in the study; differential expression profiles for human BC cell lines and tissues by molecular subtypes; enrichment scores for apoptosis and ferroptosis potential indices in human BC tissues;

characterization of FeS₂ and FeS₂-PEG₈ NCs; serum stability, in vivo optoacoustic spectra, distribution and pharmacokinetics, and thermogenesis and PCE of FeS₂-PEG₈ NCs, in vitro migration and invasion assays; therapeutic effects on primary and metastatic TNBC tumors; mRNA expression of ferroptosis-related genes; lipid peroxidation and antioxidation enzyme activities; distribution of differentially expressed genes; enrichment analysis of RNA-seq data; and cytotoxicity, hemolysis assays, and extensive investigations of short-term and long-term toxicity of FeS₂-PEG₈ NCs (PDF)

AUTHOR INFORMATION

Corresponding Authors

Ze-Xian Liu – State Key Laboratory of Oncology in South China, Guangdong Key Laboratory of Nasopharyngeal Carcinoma Diagnosis and Therapy, Collaborative Innovation Center for Cancer Medicine, Sun Yat-sen University Cancer Center, Guangzhou 510060, China; orcid.org/0000-0001-9698-0610; Email: liuzx@sysucc.org.cn

Di-Yan Wang – Department of Chemistry, Tunghai University, Taichung 40704, Taiwan; orcid.org/0000-0003-3084-6050; Email: diyanwang@thu.edu.tw

Jiang Yang – State Key Laboratory of Oncology in South China, Guangdong Key Laboratory of Nasopharyngeal Carcinoma Diagnosis and Therapy, Collaborative Innovation Center for Cancer Medicine, Sun Yat-sen University Cancer Center, Guangzhou 510060, China; Department of Radiology, Memorial Sloan Kettering Cancer Center, New York, New York 10065, United States; orcid.org/0000-0001-5934-1537; Email: yangjiang@sysucc.org.cn

Authors

Chunhua Zhao – State Key Laboratory of Oncology in South China, Guangdong Key Laboratory of Nasopharyngeal Carcinoma Diagnosis and Therapy, Collaborative Innovation Center for Cancer Medicine, Sun Yat-sen University Cancer Center, Guangzhou 510060, China

Zekun Liu – State Key Laboratory of Oncology in South China, Guangdong Key Laboratory of Nasopharyngeal Carcinoma Diagnosis and Therapy, Collaborative Innovation Center for Cancer Medicine, Sun Yat-sen University Cancer Center, Guangzhou 510060, China

Chia-Che Chang – Department of Chemistry, Tunghai University, Taichung 40704, Taiwan

Yi-Chia Chen – Department of Chemistry, Tunghai University, Taichung 40704, Taiwan

Qize Zhang – Department of Radiology, Memorial Sloan Kettering Cancer Center, New York, New York 10065, United States

Xiao-Dong Zhang – Department of Physics and Tianjin Key Laboratory of Low Dimensional Materials Physics and Preparing Technology, School of Sciences, Tianjin University, Tianjin 300354, China; orcid.org/0000-0002-7212-0138

Chrysafis Andreou – Department of Radiology, Memorial Sloan Kettering Cancer Center, New York, New York 10065, United States; Department of Electrical and Computer Engineering, University of Cyprus, Nicosia 1678, Cyprus; orcid.org/0000-0002-3464-9110

Jiadong Pang – State Key Laboratory of Oncology in South China, Guangdong Key Laboratory of Nasopharyngeal Carcinoma Diagnosis and Therapy, Collaborative Innovation

Center for Cancer Medicine, Sun Yat-sen University Cancer Center, Guangzhou 510060, China

Moritz F. Kircher – Department of Radiology, Memorial Sloan Kettering Cancer Center, New York, New York 10065, United States

Complete contact information is available at:

<https://pubs.acs.org/10.1021/acsnano.2c06629>

Author Contributions

[#]C.Z. and Z.L. contributed equally to the work. J.Y., M.F.K., D.-Y.W., and Z.-X.L. conceived and designed the experiments and co-supervised the project. J.Y. and C.Z. wrote the manuscript. C.-C.C., Y.-C.C., D.-Y.W., C.Z., and J.Y. synthesized, functionalized, and characterized the nanocrystals. J.Y., C.Z., C.A., and Q.Z. conducted optoacoustic imaging. C.Z. and J.Y. performed in vitro and in vivo experiments. C.Z., Z.L., Z.-X.L., and J.Y. investigated molecular mechanisms. X.-D.Z. and J.P. provided technical support in conducting experiments. J.Y., C.Z., Z.L., Z.-X.L., and D.-Y.W. co-analyzed the data. All authors joined the technical discussion, troubleshoot, and contributed to the result analysis. The manuscript was revised, proofread, and approved by all authors.

Notes

The authors declare no competing financial interest.

[†]Deceased August 15th, 2020.

ACKNOWLEDGMENTS

The following funding sources provided to J.Y. are acknowledged: the National Key Research and Development Program of China (2021YFF1200700), the National Natural Science Foundation of China (82071978 and 52271196), the Guangdong Natural Science Foundation (2021A1515012404), the Open Funds of State Key Laboratory of Oncology in South China (HN2022-01), and the SYSUCC start-up research funding. The National Institute of Health grants (R01EB017748 and R01CA222836), the Pershing Square Sohn Prize, and the Parker Institute for Cancer Immunotherapy supported M.F.K. financially. D.-Y.W. was financially supported by the Ministry of Science and Technology of Taiwan (MOST 109-2113-M-029-002) and Tunghai University. Z.-X.L. thanks the Program for Guangdong Introducing Innovative and Entrepreneurial Teams (2017ZT07S096) and the Tip-Top Scientific and Technical Innovative Youth Talents of Guangdong Special Support Program (2019TQ05Y351) for funding support. The authors also thank Prof. Zhen Yuan from the Faculty of Health Sciences at the University of Macau for conducting OR-PAM imaging. J.Y., C.A., Q.Z., and other former Kircher lab members are dedicated to the memory of Moritz F. Kircher, M.D., Ph.D., who was Chair of the Department of Imaging and Radiology at Dana-Farber Cancer Center but unfortunately passed away during the preparation of the manuscript. He pioneered molecular imaging and theranostics with his vision, enthusiasm, and creativity, and his brilliant mind is sorely missed.

REFERENCES

- (1) Holohan, C.; Van Schaeybroeck, S.; Longley, D. B.; Johnston, P. G. Cancer drug resistance: an evolving paradigm. *Nat. Rev. Cancer* **2013**, *13*, 714–726.
- (2) Dixon, S. J.; Lemberg, K. M.; Lamprecht, M. R.; Skouta, R.; Zaitsev, E. M.; Gleason, C. E.; Patel, D. N.; Bauer, A. J.; Cantley, A. M.; Yang, W. S.; Morrison, B., 3rd; Stockwell, B. R. Ferroptosis: an iron-

dependent form of nonapoptotic cell death. *Cell* **2012**, *149*, 1060–1072.

(3) Pu, K.; Shuhendler, A. J.; Jokerst, J. V.; Mei, J.; Gambhir, S. S.; Bao, Z.; Rao, J. Semiconducting polymer nanoparticles as photoacoustic molecular imaging probes in living mice. *Nat. Nanotechnol* **2014**, *9*, 233–239.

(4) Roberts, D. M.; Landin, A. R.; Ritter, T. G.; Eaves, J. D.; Stoldt, C. R. Nanocrystalline iron monosulfides near stoichiometry. *Sci. Rep* **2018**, *8*, 6591.

(5) Ahmad, M. B.; Tay, M. Y.; Shamel, K.; Hussein, M. Z.; Lim, J. J. Green synthesis and characterization of silver/chitosan/polyethylene glycol nanocomposites without any reducing agent. *Int. J. Mol. Sci.* **2011**, *12*, 4872–4884.

(6) Bilensoy, E. Cationic nanoparticles for cancer therapy. *Expert Opin Drug Del* **2010**, *7*, 795–809.

(7) Wei, C.; Jin, X.; Wu, C.; Brozovic, A.; Zhang, W. Carbon spheres with high photothermal conversion efficiency for photothermal therapy of tumor. *Diam Relat Mater.* **2022**, *126*, 109048.

(8) Li, L.; Yang, Q.; Shi, L.; Zheng, N.; Li, Z.; Li, K.; Qiao, S.; Jia, T.; Sun, T.; Wang, Y. Novel phthalocyanine-based polymeric micelles with high near-infrared photothermal conversion efficiency under 808 nm laser irradiation for in vivo cancer therapy. *J. Mater. Chem. B* **2019**, *7*, 2247–2251.

(9) Huang, P.; Lin, J.; Li, W.; Rong, P.; Wang, Z.; Wang, S.; Wang, X.; Sun, X.; Aronova, M.; Niu, G.; Leapman, R. D.; Nie, Z.; Chen, X. Biodegradable gold nanovesicles with an ultrastrong plasmonic coupling effect for photoacoustic imaging and photothermal therapy. *Angew. Chem., Int. Ed. Engl.* **2013**, *52*, 13958–13964.

(10) Dong, L.; Ji, G.; Liu, Y.; Xu, X.; Lei, P.; Du, K.; Song, S.; Feng, J.; Zhang, H. Multifunctional Cu–Ag₂S nanoparticles with high photothermal conversion efficiency for photoacoustic imaging-guided photothermal therapy in vivo. *Nanoscale* **2018**, *10*, 825–831.

(11) Liu, Y.; Ai, K.; Liu, J.; Deng, M.; He, Y.; Lu, L. Dopamine-melanin colloidal nanospheres: An efficient near-infrared photothermal therapeutic agent for in vivo cancer therapy. *Adv. Mater.* **2013**, *25*, 1353–1359.

(12) Sun, T.; Chen, X.; Wang, X.; Liu, S.; Liu, J.; Xie, Z. Enhanced efficacy of photothermal therapy by combining a semiconducting polymer with an inhibitor of a heat shock protein. *Mater. Chem. Front* **2019**, *3*, 127–136.

(13) Chatterjee, S.; Huang, E. H.-B.; Christie, I.; Kurland, B. F.; Burns, T. F. Acquired resistance to the Hsp90 inhibitor, ganetespib, in KRAS-mutant NSCLC is mediated via reactivation of the ERK–p90RSK–mTOR signaling network. *Mol. Cancer Ther* **2017**, *16*, 793–804.

(14) Wang, D. Y.; Jiang, Y. T.; Lin, C. C.; Li, S. S.; Wang, Y. T.; Chen, C. C.; Chen, C. W. Solution-processable pyrite FeS(2) nanocrystals for the fabrication of heterojunction photodiodes with visible to NIR photodetection. *Adv. Mater.* **2012**, *24*, 3415–3420.

(15) Zhang, X.; Li, M.; Walter, J.; O'Brien, L.; Manno, M. A.; Voigt, B.; Mork, F.; Baryshev, S. V.; Kakaliotis, J.; Aydil, E. S.; Leighton, C. Potential resolution to the doping puzzle in iron pyrite: Carrier type determination by Hall effect and thermopower. *Phys. Rev. Mater.* **2017**, *1*, No. 015402.

(16) Rimstidt, J. D.; Vaughan, D. J. Pyrite oxidation: a state-of-the-art assessment of the reaction mechanism. *Geochim. Cosmochim. Acta* **2003**, *67*, 873–880.

(17) Qi, F.; Hu, C.; Yu, W.; Hu, T. Conjugation with Eight-Arm PEG Markedly Improves the In Vitro Activity and Prolongs the Blood Circulation of Staphylokinase. *Bioconjug Chem.* **2018**, *29*, 451–458.

(18) Yang, J.; Wang, B.; You, Y.; Chang, W. J.; Tang, K.; Wang, Y. C.; Zhang, W.; Ding, F.; Gunasekaran, S. Probing the modulated formation of gold nanoparticles-beta-lactoglobulin corona complexes and their applications. *Nanoscale* **2017**, *9*, 17758–17769.

(19) Vercauteren, D.; Deschout, H.; Remaut, K.; Engbersen, J. F. J.; Jones, A. T.; Demeester, J.; De Smedt, S. C.; Braeckmans, K. Dynamic colocalization microscopy to characterize intracellular trafficking of nanomedicines. *ACS Nano* **2011**, *5*, 7874–7884.

(20) Harmsen, S.; Huang, R.; Wall, M. A.; Karabeber, H.; Samii, J. M.; Spaliviero, M.; White, J. R.; Monette, S.; O'Connor, R.; Pitter, K. L.

Sastra, S. A.; Saborowski, M.; Holland, E. C.; Singer, S.; Olive, K. P.; Lowe, S. W.; Blasberg, R. G.; Kircher, M. F. Surface-enhanced resonance Raman scattering nanostars for high-precision cancer imaging. *Sci. Transl Med.* **2015**, *7*, 271ra7.

(21) Wagner, A. L.; Danko, V.; Federle, A.; Klett, D.; Simon, D.; Heiss, R.; Jungert, J.; Uder, M.; Schett, G.; Neurath, M. F.; Woelfle, J.; Waldner, M. J.; Trollmann, R.; Regensburger, A. P.; Knieling, F. Precision of handheld multispectral photoacoustic tomography for muscle imaging. *Photoacoustics* **2021**, *21*, 100220.

(22) Dileepkumar, V. G.; Surya, P. S.; Pratapkumar, C.; Viswanatha, R.; Ravikumar, C. R.; Anil Kumar, M. R.; Muralidhara, H. B.; Al-Akara, I. M.; Mohammad, A. M.; Chen, Z.; Bui, X.-T.; Santosh, M. S. NaFeS₂ as a new photocatalytic material for the degradation of industrial dyes. *J. Environ. Chem. Eng.* **2020**, *8*, 104005.

(23) MacCuaig, W. M.; Jones, M. A.; Abeyakoon, O.; McNally, L. R. Development of Multispectral Photoacoustic Tomography as a Clinically Translatable Modality for Cancer Imaging. *Radiol Imaging Cancer* **2020**, *2*, No. e200066.

(24) Yang, J.; Wang, T.; Zhao, L.; Rajasekhar, V. K.; Joshi, S.; Andreou, C.; Pal, S.; Hsu, H.-t.; Zhang, H.; Cohen, I. J.; Huang, R.; Hendrickson, R. C.; Miele, M. M.; Pei, W.; Brendel, M. B.; Healey, J. H.; Chiosis, G.; Kircher, M. F. Gold/alpha-lactalbumin nanoprobe for the imaging and treatment of breast cancer. *Nat. Biomed Eng.* **2020**, *4*, 686–703.

(25) Yang, J.; Zhao, C.; Lim, J.; Zhao, L.; Tourneau, R. L.; Zhang, Q.; Dobson, D.; Joshi, S.; Pang, J.; Zhang, X.; Pal, S.; Andreou, C.; Zhang, H.; Kircher, M. F.; Schmitthenner, H. Structurally symmetric near-infrared fluorophore IRDye78-protein complex enables multimodal cancer imaging. *Theranostics* **2021**, *11*, 2534–2549.

(26) Roper, D. K.; Ahn, W.; Hoepfner, M. Microscale heat transfer transduced by surface plasmon resonant gold nanoparticles. *J. Phys. Chem. C* **2007**, *111*, 3636–3641.

(27) Kim, D.; Langmead, B.; Salzberg, S. L. HISAT: a fast spliced aligner with low memory requirements. *Nat. Methods* **2015**, *12*, 357–360.

(28) Pertea, M.; Pertea, G. M.; Antonescu, C. M.; Chang, T. C.; Mendell, J. T.; Salzberg, S. L. StringTie enables improved reconstruction of a transcriptome from RNA-seq reads. *Nat. Biotechnol.* **2015**, *33*, 290–295.

(29) Love, M. I.; Huber, W.; Anders, S. Moderated estimation of fold change and dispersion for RNA-seq data with DESeq2. *Genome Biol.* **2014**, *15*, 550.

(30) Subramanian, A.; Tamayo, P.; Mootha, V. K.; Mukherjee, S.; Ebert, B. L.; Gillette, M. A.; Paulovich, A.; Pomeroy, S. L.; Golub, T. R.; Lander, E. S.; Mesirov, J. P. Gene set enrichment analysis: a knowledge-based approach for interpreting genome-wide expression profiles. *Proc. Natl. Acad. Sci. U. S. A.* **2005**, *102*, 15545–15550.

(31) Luo, W.; Pant, G.; Bhavnasi, Y. K.; Blanchard, S. G., Jr.; Brouwer, C. Pathview Web: user friendly pathway visualization and data integration. *Nucleic Acids Res.* **2017**, *45*, W501–W508.

(32) Xiao, Y.; Nimmer, P.; Sheppard, G. S.; Bruncko, M.; Hessler, P.; Lu, X.; Roberts-Rapp, L.; Pappano, W. N.; Elmore, S. W.; Souers, A. J.; Levenson, J. D.; Phillips, D. C. MCL-1 is a key determinant of breast cancer cell survival: Validation of MCL-1 dependency utilizing a highly selective small molecule inhibitor. *Mol. Cancer Ther* **2015**, *14*, 1837–1847.

(33) The Cancer Genome Atlas Network. Comprehensive molecular portraits of human breast tumours. *Nature* **2012**, *490*, 61–70.

(34) Yau, C.; Esserman, L.; Moore, D. H.; Waldman, F.; Sninsky, J.; Benz, C. C. A multigene predictor of metastatic outcome in early stage hormone receptor-negative and triple-negative breast cancer. *Breast Cancer Res.* **2010**, *12*, R85.

(35) Hanzelmann, S.; Castelo, R.; Guinney, J. GSEA: gene set variation analysis for microarray and RNA-seq data. *BMC Bioinform* **2013**, *14*, 7.